Spectral computed tomography with inorganic nanomaterials: State-of-the-art

Yuhan Li[a], **Muhsin H. Younis**[b], **Han Wang**[c], **Jian Zhang**[a,d,*], **Weibo Cai**[b,*], **Dalong Ni**[c,*]

[a]School of Medicine, Shanghai University, No. 99 Shangda Rd, Shanghai 200444, PR China

[b]Departments of Radiology and Medical Physics, University of Wisconsin–Madison, WI 53705, United States

[c]Department of Orthopaedics, Shanghai Key Laboratory for Prevention and Treatment of Bone and Joint Diseases, Shanghai Institute of Traumatology and Orthopaedics, Ruijin Hospital, Shanghai Jiao Tong University School of Medicine, No. 197, Ruijin 2nd Rd, Shanghai 200025, PR China

[d]Shanghai Universal Medical Imaging Diagnostic Center, Bldg 8, No. 406 Guilin Rd, Shanghai 200233, PR China

Abstract

Recently, spectral computed tomography (CT) technology has received great interest in the field of radiology. Spectral CT imaging utilizes the distinct, energy-dependent X-ray absorption properties of substances in order to provide additional imaging information. Dual-energy CT and multi-energy CT (Spectral CT) are capable of constructing monochromatic energy images, material separation images, energy spectrum curves, constructing effective atomic number maps, and more. However, poor contrast, due to neighboring X-ray attenuation of organs and tissues, is still a challenge to spectral CT. Hence, contrast agents (CAs) are applied for better differentiation of a given region of interest (ROI). Currently, many different kinds of inorganic nanoparticulate CAs for spectral CT have been developed due to the limitations of clinical iodine (I)-based contrast media, leading to the conclusion that inorganic nanomedicine applied to spectral CT will be a powerful collaboration both in basic research and in clinics. In this review, the underlying principles and types of spectral CT techniques are discussed, and some evolving clinical diagnosis applications of spectral CT techniques are introduced. In particular, recent developments in inorganic CAs used for spectral CT are summarized. Finally, the challenges and future developments of inorganic nanomedicine in spectral CT are briefly discussed.

Keywords

*Corresponding authors at: School of Medicine, Shanghai University, No. 99 Shangda Rd, Shanghai 200444, PR China. abiaoxp@163.com (J. Zhang), wcai@uwhealth.org (W. Cai), dalongni@sjtu.edu.cn, ndl12353@rjh.com.cn (D. Ni).

1. Introduction

The recent invention of spectral computed tomography (CT) technology has sparked interest, establishing spectral CT as a new diagnostic tool derived from CT. Spectral CT is a multi-energy imaging technique using semiconductor detectors for single photon counting and energy discrimination. Dual-energy CT (DECT) involves capturing two images, one with higher tube voltage and the other with lower tube voltage. There are typically three techniques to achieve this: 1) one X-ray tube can be used while its tube voltage is rapidly changed between high and low. 2) One X-ray tube can be used with two detectors which detect different photon energies. 3) Two X-ray tubes can be used at once, with one separate detector opposite to each of the tubes in the CT gantry. The rich imaging data that is provided can be used to thoroughly understand the material or tissues being imaged. Remarkably, this data enables monochromatic energy imaging, material separation, energy spectrum curves, construction of effective atomic number maps, etc., and can therefore provide highly useful information that can not be provided by traditional CT. Moreover, monochromatic energy images in spectral CT have the advantages of decreasing beam hardening artifacts, [1,2] metal artifacts, [3,4] and improving signal-to-noise ratio (SNR) [5]. The spectral CT has been demonstrated to successfully identify and distinguish materials that have significantly different attenuation coefficients at the energies present in the two X-ray beam spectra, which could overcome the limitations of traditional single energy CT. However, it is still a challenge for spectral CT to distinguish tissues with the same or similar attenuation characteristics, such as normal tissue and lesions. Greater differentiation in spectral CT attenuation properties will help make a distinction between normal tissues and lesions [6–8]. Consequently, the increased contrast ratio among tissues is urgently required.

In clinical practice, iodine (I)-based agents are widely applied as exogenous contrast agents (CAs) for CT imaging. However, certain imaging requirements put I-based CAs at a disadvantage. For instance, the rapid circulation and short retention time of I-based CAs restrict broader applications *in vivo*. In addition, the CT value of I is close to calcium (Ca) at high kilovolt (kV) tube voltages, which means that its X-ray attenuation curve is similar to Ca at high kiloelectron volt (keV) photon energies. This can, of course, be an issue when imaging with I near bone [9]. Considering these limitations for applying I-based CAs in spectral CT, other inorganic nanoparticles are useful as CAs for spectral CT due to their X-ray attenuation properties both at low and high photon energies [10]. Besides iodine, elements with high atomic numbers, such as Nd, Yb, Lu, Hf, Re, Au, and Bi, may be superior as CAs for spectral CT. This collaboration between inorganic nanomedicine and spectral CT will bring promising prospects for widening their medical application.

This review is primarily to summarize the current advancement of spectral CT technology and inorganic nanomedicine, including the principles, types, application, and inorganic nanoparticle (NP) CAs (e.g., rare earth-based NPs, Au NPs, Bi-based NPs, etc.) of spectral CT technology, as shown in Fig. 1. With this timely and comprehensive review, we deeply believe that the collaboration of spectral CT technology and inorganic nanoparticulates will stimulate extensive further research and bring a bright future for both spectral CT and inorganic nanomedicine.

2. Principles of spectral CT

Since Roentgen discovered high-energy rays capable of penetrating biological tissue in 1895, a revolution in imaging technology has commenced [11]. In 1973, Godfrey Hounsfield originally explored CT, a technology that can obtain tomographic images of the human body using X-rays produced by X-ray tubes with voltages of typically about 100 kV peak (kVp) to 140 kVp [12]. Since then, a series of technological advancements have been made for appropriating the different energy requirements. Spectral CT is a reformed CT system with two tube voltage modes allowing simultaneous image acquisition using lower and higher-energy spectra [9,13–15].

As X-rays pass through the human body, absorption and scattering of X-ray photons by atomic electrons will reduce the intensity of the beam, a process which is referred to as X-ray attenuation [16]. Attenuation is caused by interactions between photons and matter, primarily through two different types of interaction: Compton scattering and the photoelectric effect [17–22]. In Compton scattering, an incoming X-ray photon gives some energy to an atomic electron in the outer shell, launching the electron in an energetically constrained direction, while the X-ray departs in a correlated direction. The Compton effect dominates in materials with low electron density, therefore materials with low atomic numbers (e.g., soft tissue, fat, organs, etc.). The photoelectric effect is when an X-ray photon is completely absorbed by an atomic electron in an inner shell (K-shells). The basis of X-ray imaging is thus the detection or lack of detection of photons after passing through the body, providing a measure of electron density along the path length of the photons. Thus, absorption favorably enhances image contrast, while scattering degrades image contrast, as detection of scattered photons misattributes contrast to an incorrect path. Notably, absorption via the photoelectric effect is favored with low photon energies and high atomic numbers, such as I.

Spectral CT is an imaging technology based on the attenuation of materials at K-edge energies. A drastic increase in attenuation can be observed when the energy of incident X-ray photons is slightly higher than the K-shell energy of a given atom [23]. Photons with energies just beyond the K-shell energy are substantially more likely to be absorbed than photons with energies just under the K shell energy [24]. Since the K-edge energies of different elements are different, tissues and organs with different elemental compositions could therefore be more distinguishable to X-ray of different energies. Spectral CT can therefore discriminate body tissues and organs according to different attenuation of different materials at different photon energies. For example, bone and uric acid in gout disease, cysts and calculus in organs [19,25–27]. The capability of spectral CT to distinguish between two substances is also related to the difference in absorption at low and high incident photon energies, which is related to electron density, and can therefore be an assessment for effective atomic number of substances [24,28–30]. The greater the difference in electron density, the simpler it is to separate the two substances.

By scanning one time with synchronous acquisition or rapid switching at low- and high-energy, spectral CT can simultaneously acquire a large amount of information, which can obtain base material decomposition (BMD) images, monochromatic energy images, energy

spectrum curves, and map of effective atomic number, facilitating image reconstruction through three post-processing tools - best SNR, histogram, and scatter plot [31]. By this way, it provides accurate and comprehensive information for various diseases of morphology and functional changes, and meets different clinical requirements.

At present, there are several techniques used to acquire dual-energy images, which have been developed in clinical practice. These techniques include dual source technology (dual source CT, DSCT, Siemens Healthcare), tube rapid kVp switching technology (gemstone spectral CT, GSCT, GE Healthcare; dual energy CT, DECT, Canon Medical), and double layer detector (IQon spectral CT, Philips Healthcare) (Table 1). Nevertheless, DECT can be divided into single source dual energy CT (ssDECT) and dual source dual energy CT (dsDECT) based on the type of equipment. The ssDECT uses a single X-ray tube source which is capable of having its tube voltage rapidly adjusted, which therefore allows for the use of ssDECT with some of the more recent CT advancements, such as helical CT, or with detectors such as double layer and photon counting detectors. On the other hand, dsDECT uses two X-ray tubes, each at a constant tube voltage, where the two sources and two detectors are mounted orthogonally and rotate simultaneously [24,28,32–37]. Analyzing the two X-ray spectra to achieve material discrimination primarily based on two base-material pairs (such as I and water) is generally feasible, relying on the principles of Compton scattering and the photoelectric effect [38]. Compared to DECT, multi-energy CT is generally considered to offer better energy separation and spectral measurements [39,40]. The evolution of photon counting detectors (PCDs), which offer an alternative to energy integrating detectors (EIDs), has expanded dual-energy technology to multi-energy technology, where the systems can count individual incident X-ray photons and take the measurements of their energies (Table 1) [41,42]. Photon counting CT utilizes the analysis of K-edge imaging to measure elements content, which provides the opportunity to evaluate the amount and location of multiple contrast agents (e.g., iodine and gold or iodine and bismuth). Although the decomposition system for photon counting CT is currently limited to the clinical scenario, this will be the goal of clinical applications of spectral CT (see Table 2).

3. Applications of spectral CT

As various CT vendors (such as GE Healthcare, Siemens Healthcare, Philips Healthcare) have developed spectral CT platforms, some post-processing software for intelligent diagnosis is also needed. Several clinically related spectral CT procedures including blending images, monochromatic images, energy spectrum curves, BMD images, angiography, 3D reconstruction, etc., are introduced in this section. In addition, to better understand the post-processing procedure of scanned images, clinical cases will be cited for an explanation.

3.1. Blending images

Spectral CT images are processed by collecting X-rays of two different energies to extract a range of data from different processing methods. Standardized original images using 80 kVp and 140 kVp X-rays are available for regular diagnosis [43]. Compared with 140 kVp

images, 80 kVp images typically display more absorption (Fig. 2a–b) [44]. Noise reduction can be achieved through primary reconstruction of weighted images with a blending ratio for low- and high-energy images [24,28]. The ratio of 3:7 of low- and high-energy image information (i.e., 30% weight for the 80 kVp and 70% weight for the 140 kVp image) is usually suggested to resemble conventional 120 kVp CT images (Fig. 2c) [18,45,46]. Conversely, the nonlinear blending system takes advantage of the high signal and low noise of the image, which is referred to as the "optimal contrast" (Fig. 2d) [34,47].

3.2. Virtual monoenergetic images

Virtual monoenergetic images are reconstructed by combining low- and high-energy X-ray scanning data, with a wide range of X-ray energies (from 40 to 190 keV) [48,49]. The iodine enhanced image is pronounced in low energy X-ray scanning on the basis of strengthening beam-hardening artifacts and image noise [18]. The SNR of iodine rises gradually at energies of 40–70 keV [9]. It is possible to compensate for metal artifacts by using increased keV; however, iodine contrast is hampered with increasing keV [50,51]. Taking angiography as an example, the enhanced image has higher density and more artifacts compared to the plain image at 50 keV. As shown in Fig. 3, there is decrease of artifacts and decreased enhancement of vascular tissues with increasing energy (in 10 keV steps) [52].

3.3. Energy spectrum curve

The spectral CT workstation allows for advanced post-processing analysis. Technicians outline circular region of interest (ROI) on the slices of lesion and normal tissue for reference [53]. After ROI information is collected, a spectral attenuation curve is automatically produced to show the attenuation value of the substance (in Hounsfield units, HU) as a function of energy (across 40–190 keV), which is referred to as an energy spectrum curve or HU curve [54–56]. The comparison of an unknown sample to known materials is useful for qualitative analysis of the ROI [57]. Take the abdomen scan in Fig. 4a as an example. After enhancement with I-based CAs (red arrow), hyperdense areas in the left kidney (green arrows) and hypodense areas in the right kidney (blue arrows) can be differentiated by sketching an HU curve. Both renal lesions are parallel to non-enhancing gallbladder fluid (dark blue arrows), demonstrating that they were avascular. A right kidney lesion with attenuation similar to gallbladder fluid indicates a cyst rather than a mass. The four curves of attenuation were compared to each other to define the ultra-dense look of the left renal lesion as proteinaceous cysts or hemorrhagic rather than iodine enhancement (Fig. 4b) [13].

3.4. Base material decomposition images

Given its innovative, reliable, prospective diagnosis and advanced post-processing tools, spectral CT has been used in base material decomposition (BMD) [58–60]. The composition of substance can be qualitatively defined by refining calculation of attenuation value among low- and high-energy data sets with a primitive data field [58]. One of the most significant values of material definition is the capability to produce BMD images. By decomposing the different proportional contributions of each species in the base material pair, the BMD image can be derived, such as an iodine map (water-free) or a water map (iodine-free) [61]. Recently, the base-material pairs for BMD images have been extended to not only water/

iodine images, and Ca/iodine images, but also to Ca/gout images [62–68]. Take the left tibia images in Fig. 5a as an example. Initially, the area of the white arrow was suggested to possibly a periosteal osteosarcoma due to dystrophic calcifications on conventional CT scans. Then, spectral CT was used to accurately assess uric acid (green) by means of base-material separation, which eliminates the requirement for biopsy (Fig. 5b–d) [58].

3.5. Angiography and Three-dimensional reconstruction

Angiographic delineation can be demonstrated by using the bone-removal technique from the BMD [69]. Volume-rendered (VR) and multi-planar reconstruction (MPR), as well as maximum intensity projection (MIP), are combined into three-dimensional (3D) reconstruction images [70,71]. The application of 3D reconstruction allows better visualization of subtle anatomical structures and variations without surgical intervention [72]. Furthermore, it has the advantages of clear, intuitive, and high spatial resolution, which is of great significance for the preoperative evaluation of vascular stenosis, calcification, and obstruction [73,74]. Multifarious lesions can be better revealed by 3D rendered images, and relatively complex dimensional evidence can be freely displayed to radiologists with images of coronal, sagittal, axial views, or views from any direction [75]. For example, in the head scan in Fig. 6a, the volumes of bone, teeth, soft tissue, and skin are removed to calculate the iodine content after vascular enhancement with angiographic and 3D reconstruction image [25]. With aortic angiography and the bone removal technique in Fig. 6b, it was noted that stenosis of the right internal carotid artery becomes obvious, whereas the overlay of bone made identification of the lesion tedious in conventional 3D images as in Fig. 6c.

In summary, spectral CT demonstrates an evolving field of CT systems, which can be broadly utilized in the clinical setting, and will continue to be developed in the future [76]. Moreover, spectral CT possesses the above compelling advantages for radiologists and patients. However, the main challenge that must be met for spectral CT is to expand its breadth of specific inorganic contrast media to create more sensitive imaging protocols [77].

4. Spectral CT Nano-sized contrast agents

Contrast agents (CAs) are among the most commonly used drugs in medical imaging. CAs are administered to increase or decrease the density of specific tissue, where the former is referred to as positive enhancement, and the latter is referred to as negative enhancement [7,78]. Common CAs in CT include Barium sulfate suspensions ($BaSO_4$) and small-molecule iodinated compounds [11,79]. However, these CAs have their drawbacks and that limits their use. $BaSO_4$ is only used in gastrointestinal (GI) imaging due to the biotoxicity of Ba^{2+}. Iodinated CAs have relatively short circulation time [20,80–83]. Furthermore, patients who are allergic to iodine will feel uncomfortable owing to its extraordinary osmotic pressure and viscosity [84,85]. Importantly, spectral CT lacks specific CAs, even though numerous inorganic NPs have been researched for imaging or biomedical application [86,87]. Numerous favorable characteristics of NPs (e.g., high surface area to volume ratios, facile surface function modifications, great contrast effectiveness, and stabilizing biocompatibility) make them appealing in imaging, diagnosing, and treating diseases [88–91]. Typically, elements with higher atomic numbers and K-edge values, such

as ytterbium, lutetium [92–95], hafnium, tantalum, tungsten, rhenium, gold, bismuth, etc., are employed as spectral CT imaging CAs [41,96].

4.1. Iodine-based contrast agents

Iodine (I) is one of the widely used non-metallic CAs, with an atomic number of 53, a relative atomic mass of 126.9, and a K-edge value of 33.17 keV [97]. From the first generation of sodium iodide in 1920 to non-ionic CAs currently used, such as iohexol, ioversol, etc., scientists have dedicated themselves to continuously optimizing products over the past 100 years [98–100]. To date, I-based materials remain the most extensively used CAs for X-ray imaging.

Allphin et al. transplanted soft tissue sarcomas in $Rag2^{+/-}$ and $Rag2^{-/-}$ mice to mimic different lymphocyte burdens [101]. Mice accepted radiation therapy to prompt lymphocyte infiltration, followed by injection of a liposomal iodinated (Lip-I) CA. Mice were imaged using conventional micro-CT with EID and spectral micro-CT with PCD to acquire images of PCD, EID, I, photoelectric effect (PE), and Compton scattering (CS) (Fig. 7a). Coronal views of $Rag2^{-/-}$ and $Rag2^{+/-}$ mouse exhibit multicolor images of Lip-I accumulation in the tumor by the decomposition results (Fig. 7b). By quantifying the mean Lip-I concentration in the tumors, it was shown that $Rag2^{+/-}$ mice with lymphocytes were leakier than the tumors of $Rag2^{-/-}$ mice, indicating that the spectral approach may assist tumor stratification in cancer treatment.

Although iodine-based CAs have played an important role in the field of CT imaging, it is undeniable that there are some problems with I-based materials in their application. Firstly, the rapid circulation and short retention time of I-based CAs restrict broader applications *in vivo*. To prolong the short imaging time and alleviate patient discomfort, nanoscale I-based CAs, such as emulsions [102,103], micelles [104], polymers [105,106], and liposomes [107], have been fabricated [20,90,107–113]. For example, Balegamire et. al. designed a polymeric I-based NP for CT and spectral photon counting CT (SPCCT) that can remain for several hours in the cardiovascularsystem, before accumulating in the liver and spleen [114]. Secondly, the CT value of iodine decreases sharply with the increase of incident photon keV, and only increasing the dose of CA can retain the original CT value [115]. Nevertheless, CAs containing high-Z elements are promising candidates for positive enhancement. The first reason for this is that using high-Z elements, whose CT value changes are more robust at high energies, can improve image quality at less concentration of CAs. The second reason is that CAs with high-Z elements could also reduce the overall radiation exposure dose to patients. The final is that easily modified surfaces can significantly enhance the versatility of materials, which would be beneficial for multimodal imaging and drug-loaded therapy. Faced with the needs of radiologists and patients, researchers insist on exploiting more suitable CAs to meet these challenges.

4.2. Rare earth-based nanoparticles

4.2.1. Yb-based nanoparticles—Ytterbium (Yb) is a lanthanide metal with an atomic number of 70 and a relative atomic mass of 173. Its K-edge value is 61.3 keV. This is quite a favorable value because, according to previous reports, the image quality of spectral CT

monoenergetic level between 65 and 75 keV can be maximized compared to conventional single-energy CT images at 120 kVp [49,116]. Therefore, a material with a K-edge value between 65 and 75 keV will exhibit good contrast. Yb chelates have been considered as another choice for blood pool contrast media and have demonstrated to be safer [117].

One interesting instance of the use of a Yb spectral CT CA is in imaging of atherosclerosis. Atherosclerosis is an inflammatory disease, which is mainly caused by the lipid and fiber accumulate in the arteries [118–121]. Over time, atherosclerotic plaque will endure accumulating and block blood vessels in the late period, leading to ischemia, infarction, stroke, and other diseases, which are the most common causative factors of cardiovascular disease (CVD) [122]. CVD is the leading cause of death in the world, and it is extremely urgent to make effective diagnoses for CVD patients. Considering the SNR of the image, Pan et. al. employed ytterbium nanocolloids (YbNC) for spectral CT imaging [123]. The soluble organic Yb complex is packaged in phospholipids, producing YbNCs with diameters of approximately 200 nm for blood pool imaging (Fig. 8a). In the *in vitro* experiments, different concentrations of YbNC, agarose, and calcium chloride ($CaCl_2$) were marked with different colors *via* spectral CT processing technology (Fig. 8b–d). The *in vivo* study was conducted with the cross-section of heart. There was almost no change in density in the traditional CT image (Fig. 8e), and a point that differs from the surrounding bones was detectable *via* spectral CT image (Fig. 8f–h). This work indicated that Yb has good K-edge imaging properties and performs magnificently in spectral CT of blood pool imaging, revealing its potential in detecting CVD plaques.

Bone micro-injuries typically appear in the form of bone cracks, which can lead to fractures if they are allowed to develop. Nevertheless, normal bones and damaged bones have similar elements and HU values, which are frequently unable to be distinguished using traditional X-ray imaging methods. Therefore, the development of effective preoperative diagnostic tools could play a critical role in practice [124]. Wang et al. synthesized the targeted Yb-based NPs (YbNP@SiO_2-NTA) [125], which consists of a shell-core structured NP covered by SiO_2 (YbNP@SiO_2) with bare amino groups that are united with a the chelator N-nitrilotriacetic acid (NTA) to finally form YbNP@SiO_2-NTA (Fig. 9a). NTA is used as a Ca chelator that can specifically bind to Ca^{2+} at the site of bone cracks for active targeting. *Ex vivo* experiments showed that healthy and damaged bones were detected by GSCT. HU values of both healthy and damaged bone were the same at 40 keV, while the signal difference between the first and second cracks targeted with YbNP@SiO_2-NTA and the third untargeted crack gradually enlarged with the increased keV, demonstrating the sensitivity of GSCT and the great targeting of YbNP@SiO_2-NTA (Fig. 9b–g). Encouraged by this conclusion, YbNP@SiO_2-NTA was utilized for spectral CT and conventional CT. YbNP@SiO_2-NH_2, which is unable to target bone cracks, was set as a control to be imaged by spectral CT in rat legs (Fig. 9h). As expected, GSCT with YbNP@SiO_2-NTA offered specific imaging. By measuring the iodine density and CT value, the material accumulated maximum concentration at 24 h, and then the signal started to decrease slowly (Fig. 9i, j). These results suggested that GSCT was capable of accurately differentiating between healthy and damaged bone with YbNP@SiO_2-NTA contrast agent.

4.2.2. Lu-based nanoparticles—Lutetium (Lu) is the last metal element in the lanthanide series and is the hardest and densest metal of the rare earth elements, with an atomic number of 71 and a relative atomic mass of 175. It is also known to have excellent X-ray absorption properties in CT imaging as well as unique upconversion luminescence properties, which have become increasingly interesting in researches [126,127].

Osteosarcoma is a primary bone tumor with a high morbidity and poor prognosis in children. If the patient is not treated accurately, serious consequences may occur and amputation may be necessary. Regrettably, the current diagnosis of these diseases is not ideal [128]. Osteosarcoma is always near or inside bones, and spectral CT has difficulty discriminating between bone and tumors. This is because the HU levels of iodine and Ca are similar at high keV after enhancement (Fig. 10b). Bu and co-workers synthesized polyethylene glycol (PEG)-NaLuF$_4$:19 % Yb^{3+}/1%Er^{3+} (Lu-based UCNPs) as CAs for GSCT (Fig. 10a) [129]. Pig bone is supplied as an *ex vivo* model, which was inserted *via* two tubes with iohexol on the left and Lu-based UCNPs on the right. It is known from GSCT scan data (i.e., single energy images, material separation images) that Lu-based UCNPs exhibit superior and unique imaging effects when compared to iohexol, showing enormous potential for diagnosis of osteosarcomas (Fig. 10c–l).

To further explore the potential of GSCT CAs in a more complex environment *in vivo*, osteosarcoma was implanted on both legs of a rat and imaged (Fig. 10m–t). In water-based (Ca) images, the processing software removes attenuating substances that are the same or similar to bones, and only leaves water-based substances (Fig. 10p, s). In the Ca (water) image, the software removes the water-based image, hence retaining the bones and iohexol (Fig. 10q, t). This study not only demonstrates the superior imaging characteristics of Lu-UCNPs compared to iohexol in this context, but also demonstrates separation of Lu-UCNPs, iohexol, and bone in imaging, in order to distinguish between osteosarcomas with CA accumulation and bones.

4.3. Hf-based nanoparticles

Hafnium (Hf) is a transition metal with an atomic number of 72, whose relative atomic mass is 178.49, and K-edge value is65.3 keV. With a high atomic number and high density, Hf is mainly applied for radiosensitization and X-ray imaging owing to its high degree of X-ray absorption [130]. In addition, the K-edge absorption value of Hf is close to 70 keV, which can provide great overall performance for clinical CT imaging [131]. However, there are few studies on Hf as CAs for spectral CT.

Ostadhossein et al. synthesized smaller targeted HfO$_2$@NTA NPs (Fig. 11a) for use as a CA [132]. As part of an *in vitro* experiment, micro-CT images of control samples, immersed in targeted HfNPs, and non-targeted HfNPs were obtained (Fig. 11b). Subsequently, spectral CT was performed, showing the targeted NPs have accumulated at the surface of the bone injury (Fig. 11c). Micro-cracks were induced in the left leg of rats, and the same other three groups were set up. The NPs were injected into the leg intramuscularly, followed by spectral CT scans at 30 min and 5 h respectively. For the targeted group, the NPs covered at the bone micro-injury site were observed at 30 min, and more NPs enriched at the site with time increasing to 5 h, which is opposite contrast to the non-targeted group (Fig. 11d). The

accumulation of NPs in the legs can be captured by 3D reconstruction and differentiated from surrounding tissues and normal bones (Fig. 11e, g). Fig. 11f is a TEM image of the muscle sites after euthanasia of the targeted HfNP group. Notably, dispersed sub-5 nm targeted NPs remained in the sarcoplasmic reticulum, confirming biostability. In conclusion, spectral CT with Hf-based CAs can be a more powerful technique of materials identification while also providing an innovative detection method for orthopedic physiological anatomy.

Based on extensive experience in photon counting CT, Ostadhossein et. al. designed patient friendly probiotic biomimetic capsules packed with HfO_2 NPs for color GI tract imaging (Fig. 12a,b) [133]. By evaluating the X-ray attenuation of Hf at different energy bins, the graph shows a clear enhancement in attenuation in the third energy bin (E3, 65–80 keV), which relates to the K-edge energy of Hf (Fig. 12c). Sprague Dawley rats were given oral gavage to further explore the imaging application of HfO_2 *in vivo*. Fig. 12d and e showed the effect of overlaid energy bins without or with HfO_2 material, respectively. The 3D view of the accumulation of HfO_2 NPs and the decomposition of the material indicate that Hf and bone are present independently, and the accumulated concentration values of the material are recorded (Fig. 12f–h). To simulate a more complex GI environment, rats were fed before being gavaged. In this case, the material decomposition (MD) procedure was run in spectral CT using four base species: Hf, HA (representing Ca), lipids, and water (Fig. 12i–m). Thus, spectral CT images could effectively delineate Hf, lipids, soft tissues, and HA signals. Overall, it is demonstrated that inorganic Hf-based NPs can be applied in the GI system for K-edge imaging.

4.4. Ta-based nanoparticle

Tantalum (Ta) is a transition metal element with an atomic number of 73, a relative atomic mass of 180.9, and a K-edge of67.4 keV. Ta has been used in medical devices for tissue repair due to its strong corrosion resistance. Tantalum oxide is known to be chemically inert in the intestinal environment, which allows for viability as a material for visualization of the GI tract [134]. Previously, preliminary reports have demonstrated the imaging capabilities of tantalum [135–137].

Lambert et al. compared the CA performance of tantalum oxide NPs (TaNPs) and iopromide in a pig model used to simulate obese patients [137]. The CT values of TaNPs in blood vessels were higher than those of iopromide at different time points in the three liver and abdominal aorta sizes (102, 119, 137 cm girth) (Fig. 13a and b). In the CT axial view of the liver, TaNPs exhibit better image quality than iopromide (Fig. 13c–h). For obese patients who may require higher CA doses or higher radiation doses, the use of Ta-based CAs with higher SNR has the potential to improve the quality of their CT vascular images, thereby increasing the diagnostic efficiency for this population.

4.5. W-based nanoparticle

Tungsten (W) is a metal with an atomic number of 74, a relative atomic mass of 183.84, and a K-edge of 69.5 keV. Tungsten has stable chemical properties and is suitable for GI and angiographic research. Furthermore, tungsten-based NPs can also be used for imaging or photothermal therapy (PTT). For example, Dong et al. synthesized manganese tungstate

($MnWO_4$) CA for CT/MRI multimodal imaging [138], and Liu et al. prepared WO_{3-x} NPs that could be used for tumor CT imaging and near-infrared excited PTT [139].

Mongan et al. established two groups of animal models to evaluate the feasibility of DECT to differentiate between two simultaneously acting CAs [140]. The first rabbit received intravenous injection of iodinated CAs and oral administration of bismuth subsalicylate to delineate the intestinal wall and lumen (Fig. 14a–d). In DECT, CAs can be divided into iodine (intravascular) and bismuth (intestinal) based on material density. The second rabbit was initially injected with a tungsten cluster CA followed by iohexol to allow imaging of the venous phase with tungsten and the arterial phase with iodine during the scan (Fig. 14e–h). There was a near perfect collocation between venous and arterial phase images, suggesting the potential of DECT for vascular imaging of different CAs injected at different times.

4.6. Re-based nanoparticle

Rhenium (Re) is a rare metal with an atomic number of 75, a relative atomic mass of 186, and a K-edge value of 71.7 keV. Re not only has a high atomic number, but also exhibits remarkable photoacoustic and near-infrared light absorption effects. ReS_2 is reported as a potent drug with a reassuring safety profile [141–143], and low toxicity as a radiotherapy sensitizer [144–146]. Hence, ReS_2 NPs are interesting candidates for researchers to explore multifunctional applications.

Early diagnosis of GI diseases is extremely important for a good prognosis. Strict requirements are imposed on imaging technology, due to the complex environment of the GI tract with food residues or digestive juices inside, and with functional organs (e.g., liver and spleen) nearby [147]. The large density of Re could effectively reduce GI motility and small artifacts. ReS_2 NPs were synthesized by Wang et al. for radiosensitization, CT imaging of the GI tract or tumor, and photothermal therapy (Fig. 15a) [143]. Compared with the sudden decreasing trend of iohexol, the attenuation due to ReS_2 declines slowly as photon energy increases, which suggests that the X-ray attenuation of ReS_2 is more stable (Fig. 15b, d). For *in vivo* GI, ReS_2 NPs were administered to mice orally and then scanned in real time. The shape of the stomach and small intestine can be clearly delineated at 5 min. ReS_2 CAs are excreted from the body at 72 h, which guarantees biological clearance (Fig. 15c). In addition, the mice underwent spectral CT scanning after taking ReS_2 or iohexol for 5 min. The signal of ReS_2 CAs exhibited a trifling decrease with increasing single energy, but the signal of iohexol weakened sharply (Fig. 15c). The *in vivo* results were in accordance with those *in vitro*. Furthermore, in *in vivo* tumor imaging, iohexol displays a similar X-ray attenuation trend as surrounding tissues at high energy, while ReS_2 has relatively constant imaging capability both at low or high energies (Fig. 15e).

4.7. Au-based nanoparticles

Gold NPs (AuNPs) have received much attention due to their unique physical and chemical properties [148,149], such as photothermal therapy, photoacoustic imaging [150], and chemotherapy, to name a few. The atomic number of Au is 79 and its K-edge value is 80.7 keV. This high atomic number also makes it more suitable for imaging over I [151]. Furthermore, Au is nontoxic within a certain concentration range due to its physical

inertness [152,153]. To the best of our knowledge, the surface of the Au is easily modified by a series of chemical and biological agents such as targeted materials, chemotherapeutics, imaging dyes, etc., to achieve more desirable effects [154].

Liposomal iodine (Lip-I) and AuNPs were used by Clark's team to quantity the fractional blood volume (FBV) and permeability of blood vessels [155]. Lip-I and AuNPs were chosen based on their high atomic numbers, spectral K-edge absorption, and biosafety (Fig. 16a) [156]. Models of water, different concentrations of Au, and I were constructed *in vitro* to verify the decomposition and filtration performance of DE micro-CT (Fig. 16b), which focused on *in vivo* characterization of soft tissue sarcoma (Fig. 16e). The vasculature is obviously visible on day 1 after AuNP injection. Extravasation of AuNPs from surrounding tissues of tumors could be observed on both day 2 and day 4. Following Lip-I injection, DE could be used to decompose species to measure the FBV of the tumor (Fig. 16c) and the extravasation concentration (Fig. 16d). On day 6, the AuNPs and Lip-I were observed in tumor tissue. The white arrows indicated increased doses of AuNPs and Lip-I, in bright contrast to the previous injections (Fig. 16e). The DE micro-CT based on AuNPs and Lip-I is demonstrated to be an efficient tool for noninvasive evaluation of tumor vascular. Since DE micro-CT and clinical DE have similar systems, this assessment modality is expected to translate well to the clinic.

Similar to Clark's wishes, Moghiseh et. al. performed a non-invasive assessment in tumors using spectral CT with gold-labeled antibodies targeting lymphoma and breast cancer cells [157]. The conjunction of spectral CT with gold NPs in this study can provide a valuable reference for accurate detection of tumor heterogeneity, size, and location, enabling effective personalized cancer therapy. In another work, Cormode et al. encapsulated the gold core with high density lipoprotein (Au-HDL), followed by coating hydrophilicity phospholipid and adding rhodamine lipids (Fig. 17a) [158]. An arterial model was simulated *in vitro* by placing raw meat, meat processed with calcium phosphate, Au-HDL, and iopamidol, into tubes (Fig. 17g). In this study, spectral CT was demonstrated to sensitively separate Au, I, and Ca (Fig. 17h–l), which could not be observed by conventional CT (Fig. 17g). The apo E-KO atherosclerosis mouse model was used for further specific macrophage imaging. 24 h after Au-HDL injection, the aorta of these mice exhibited Au-HDL signal in spectral CT while there was no significant contrast in conventional CT (Fig. 17b–d). In the subsequent experiment, an additional dose of iodinated CAs was administered 24 h after Au-HDL injection. As shown in Fig. 17e, only varying degrees of attenuation was seen on traditional CT images. Spectral CT image analysis discovered that the signals in the lumen and plaque were iodinated CAs and Au-HDL respectively, and were not disturbed by surrounding bone (Fig. 17f). Based on this work, the ability of spectral CT to visualize and differentiate Au-HDL, iodine, and calcification in atherosclerosis was preliminarily demonstrated. In subsequent work, Si-Mohamed et. al. build upon the animal experiments with *in vivo* imaging before injection and 5 min, 45 min, 1 day, and 2 days after injection of AuNPs [159]. After the end of aortic angiography, iodinated CA (iomeprol) was injected again to demonstrate the feasibility of multicolor imaging in quantifying macrophage burden, calcification, and stenosis in atherosclerotic plaques.

Cuccione and co-workers used SPCCT to monitor and measure AuNPs-labeled therapeutic cells in iodine-based NPs-labeled scaffolds transplanted into rats with brain damage [42]. In another study, Si-Mohamed et. al. prepared models of eleven tubes where two contrast agents (i.e., gadolinium, I, or gold NPs) were arbitrarily mixed in different ratios, and used SPCCT to perform multicolor quantitative imaging of water, gadolinium, I, and gold [160]. In summary, there have been many previous studies in which SPCCT can be used to qualitatively and quantitatively analyze two or multiple CAs (i.e., iodine, gadolinium, gold, or bismuth NPs) [161–166].

4.8. Bi-based nanoparticles

Bismuth (Bi) is a stable element with an atomic number of 83, relative atomic mass of 209, and K-edge value of 90.5 keV. Bi has stable chemical properties and has been broadly used in GI therapy and X-ray imaging [77,167]. Recently, Bi [168–175], Bi_2S_3 [176–183], Bi_2Se_3 [184–188], BiOX (X = Cl, Br, I) [177,189], and other Bi-based materials, have been extensively explored in oncology [190,191]. It is worth mentioning that Bi is one of the cheapest heavy metal elements, which gives it more practical significance in medical applications [192,193].

The liver is known as the "chemical plant" of the body because it removes toxins from the body. The liver has a stronger ability to regenerate than other organs, and many diseases can be avoided or even reversed if diagnosed and treated promptly [194–198]. Liver fibrosis is a chronic disease that can lead to more serious diseases such as cirrhosis and liver cancer [199]. While traditional diagnostic methods rely on invasive biopsy, the latest spectral CT offers hope for the non-invasive diagnosis of liver fibrosis [200,201].

Wu et al. synthesized BiF_3@polydopamine@hyaluronic acid (BiF_3@PDA@HA) nanoprobes (NPs) that specifically bind to fibrotic tissues (Fig. 18a) [202]. Obviously, distinguishing a low concentration of Bi is difficult for conventional CT, however, it is possible with spectral CT (Fig. 18b–d). Liver fibrosis mice (targeted group) and healthy mice (control group) were compared using spectral CT and conventional CT *in vivo*. The BiF_3@PDA@HA NPs aggregated only in areas of liver fibrosis, while they were not expressed in healthy mice (Fig. 18f–g). As shown in Fig. 18f–g, the CT value change of the targeted group reached its maximum at 30 min (red dotted area). The CT value of the ROI decreases with the increase of photon energies, which is also consistent with the HU curve results (Fig. 18e, h). In summary, the BiF_3@PDA@HA NPs exhibit excellent targeted imaging capabilities in spectral CT for diagnosis of liver fibrosis.

Similar to Cormode's work [158], imaging of arteriosclerosis *via* spectral CT has also been attempted by Pan et al. [203]. Fibrin-targeted Bi-enriched K-edge nanocolloids (NanoK) were synthesized based on the different attenuation properties of Bi and Ca (Fig. 19a). *In vitro* research mimicking the physical condition of humans showed that control nanocolloids (ConNC) cannot be detected in spectral CT (Fig. 19c, e). In contrast, the NanoK targeted in a thrombus could be differentiated from calcified tissue by K-edge images (Fig. 19d, f). In the rabbit experiments *in vivo*, a small thrombus bound to NanoK targeting could be detected, indicating the high precision of spectral CT and the targeting specificity of

NanoK (Fig. 19b). The progress of Bi-based NanoK on spectral CT provides new insights for cardiology, such as the detection and quantification of coronary plaques.

5. Conclusions and future perspectives

In summary, DECT and spectral CT embody an evolving field of radiology. Technical approaches to acquire dual-energy data, including sequential scans, rapid switching of the single X-ray tube, single X-ray tube and double detector, and dual X-ray sources. Thus, dual-energy CT allows for construction of monochromatic energy imaging, energy spectrum curves, bone removal in angiography, material separation, and construction of effective atomic number maps, among other capabilities. On the other hand, spectral CT uses semiconductor detectors for single photon counting and energy discrimination. Spectral CT represents an emerging technology that enables the measurement and differentiation of more than two K-edge energies, such as the simultaneous imaging of two CAs, which will play an important role in disease staging and classification.

Currently, one of the most advanced uses of dual-energy and multi-energy imaging is the formation of low-and high-keV monoenergetic images, as well as blending images, which can better visualize physiological organizations, improve ROI area contrast, and reduce possible metal artifacts [51,204]. The BMD images and energy spectrum curves are robust for the assessment of substance properties, but the range of clinical applications must be expanded. The 3D reconstructed images endow the ROI with high-resolution spatial anatomical details, improving accuracy by identifying and eliminating extraneous structures. The development of dual-energy and multi-energy CT has moved beyond the bend, with more advanced devices and CAs in development.

Although iodine is still the most popular CA in clinical practice, its application in dual-energy and multi-energy CT is limited due to its comparatively low K-edge energy. At the same time, novel inorganic NPs with high atomic numbers composed of Yb, Lu, Hf, Ta, W, Re, Au, and Bi-based nanomaterials, have been extensively investigated as spectral CT CAs. Their high atomic numbers award these inorganic NPs with brilliant X-ray attenuation. These nanomaterials also exhibit important chemical properties such as high stability and easy modification [205]. Despite significant advances at the laboratory stage, there is still a long way to go for the application of spectral CT-specific CAs in the clinic [206–208].

Notably, CT CAs are used in diagnosis of an extensive range of diseases, which means the safety requirements are more stringent than in other situations. The design of NP CAs includes several stages: clinical requirements, conceptual design, *in vitro* testing, *in vivo* testing, and finally to clinical trials. While there are no easy answers on how to become a qualified CAs candidate, some initial suggestions for where to go next are as follows:

1. Size requirements for NPs. The optimal size of NPs would be between 15 and 200 nm [112]. The NPs smaller than 15 nm may be rapidly cleared by the kidneys, which would reduce their concentration to reach target organs. The NPs larger than 200 nm may be degraded by macrophages in the liver and spleen. At the same time, studies combining the size and shape of NPs with distribution and

pharmacokinetics *in vivo* are critical, because the distribution, degradation, and metabolism in living organisms are important for the safe use of drugs.

2. Surface modification of NPs. Surface modification can not only control the aggregation of NPs, but also help to improve biocompatibility and even realize the multi-functionalization of NPs. If administered intravenously, the imaging agent need to be effective for individualized imaging. In order to improve targeting of NPs, targeted modification of the NPs' surface is necessary. In addition, the unexpected effects may be achieved by exploiting the properties of the NPs themselves or using NPs to carry therapeutic drugs on their surface, enabling the integration of diagnosis and treatment together.

3. Cost of new CAs. The cost and synthetic route of NPs should be attended to, as large-scale doses are often involved for a successful CT CA. Gold is the most attractive candidate, but its price is also relatively high. Other relatively inexpensive elements such as Bi and Ta are also on the watch list. In addition, the synthetic route of NPs must be unified and stream-lined [209]. Inorganic nanomedicine will require the production of several tons of NPs per year once the research moves into clinical application.

This review article focused on the overview of DECT and spectral CT and its proprietary inorganic nanomedicine. While there are still issues to be solved, there is no denying that this new technology has brought new challenges and opportunities to imaging. From the perspective of basic disciplines, more properties of inorganic nanomaterials can be discovered with the help of spectral CT, and the diagnostic and applicable scope of spectral CT can be expanded with the application of inorganic NP-based CAs [210]. From the clinical perspective, the combination of spectral CT and inorganic nanomedicine can diagnose diseases more accurately and guide preoperative, intraoperative, and postoperative evaluations more comprehensively. Continued research and innovation of new CAs will enable new material functional designs, increase the quality of images, enhance our knowledge base, and inspire new ideas. In general, this work is a multidisciplinary alliance that requires input from physics, computers, chemistry, biology, medicine, pharmacology, and more, but the future is promising.

Acknowledgement

References

[1]. Kamiya K, Kunimatsu A, Mori H, et al. , Preliminary report on virtual monochromatic spectral imaging with fast kVp switching dual energy head CT: comparable image quality to that of 120-kVp CT without increasing the radiation dose [J], Jpn. J. Radiol 31 (4) (2013) 293–298. [PubMed: 23408047]

[2]. Stolzmann P, Winklhofer S, Schwendener N, et al. , Monoenergetic computed tomography reconstructions reduce beam hardening artifacts from dental restorations [J], Forensic Sci. Med. Pathol 9 (3) (2013) 327–332. [PubMed: 23512303]

[3]. Eric Pessis RC, Sverzut Jean-Michel, Bach Fabienne, Rodallec Mathieu, Guerini Henri, Feydy Antoine, DRAPé Jean-Luc, Virtual Monochromatic Spectral Imaging with Fast Kilovoltage Switching: Reduction of Metal Artifacts at CT, RadioGraphics 33 (2) (2013) 573–583. [PubMed: 23479714]

[4]. Tanaka R, Hayashi T, Ike M, et al. , Reduction of dark-band-like metal artifacts caused by dental implant bodies using hypothetical monoenergetic imaging after dual-energy computed tomography [J], Oral Surg. Oral Med. Oral Pathol. Oral Radiol 115 (6) (2013) 833–838. [PubMed: 23706923]

[5]. Lam S, Gupta R, Levental M, et al. , Optimal Virtual Monochromatic Images for Evaluation of Normal Tissues and Head and Neck Cancer Using Dual-Energy CT [J], AJNR Am. J. Neuroradiol 36 (8) (2015) 1518–1524. [PubMed: 26021623]

[6]. Lusic H, Grinstaff MW, X-ray-Computed Tomography Contrast Agents [J], Chem. Rev 113 (3) (2012) 1641–1666. [PubMed: 23210836]

[7]. Mattrey RF, Aguirre DA, Advances in contrast media research [J], Acad. Radiol 10 (12) (2003) 1450–1460. [PubMed: 14697013]

[8]. Krause W, Delivery of diagnostic agents in computed tomography [J], Adv. Drug Deliv. Rev 37 (1–3) (1999) 159–173. [PubMed: 10837733]

[9]. McCollough CH, Leng S, Yu Lifeng, Fletcher Joel G., Dual-and multi-energy CT: Principles, Technical Approaches, and Clinical Applications [J], Radiology 276 (3) (2015) 637–653. [PubMed: 26302388]

[10]. Huang HC, Barua S, Sharma G, et al. , Inorganic nanoparticles for cancer imaging and therapy [J], J. Control. Release 155 (3) (2011) 344–357. [PubMed: 21723891]

[11]. Yu SB, Watson AD, Metal-Based X-ray Contrast Media [J], Am. Chem. Soc 99(9) (1999) 2353–2377.

[12]. Hounsfield GN, Computerized transverse axial scanning (tomography): PartI. Description of system [J], Br. J. Radiol 46 (552) (1973) 1016–1022. [PubMed: 4757352]

[13]. Silva Alvin C., Morse BG, Hara Amy K., Paden Robert G., Hongo Norio, Pavlicek William. Dual-Energy (Spectral) CT: Applications in Abdominal Imaging [J], RadioGraphics 31(4) (2011) 1047–1050.

[14]. Elbakri Idris A., Fessler S M. Jeffrey A. Statistical Image Reconstruction for Polyenergetic X-ray Computed Tomography [J], IEEE 21(2) (2002) 89–99.

[15]. Roessl E, Proksa R, K-edge imaging in x-ray computed tomography using multi-bin photon counting detectors [J], Phys. Med. Biol 52 (15) (2007) 4679–4696. [PubMed: 17634657]

[16]. Prado CM, Heymsfield SB, Lean tissue imaging: a new era for nutritional assessment and intervention [J], JPEN J. Parenter. Enteral Nutr 38 (8) (2014) 940–953. [PubMed: 25239112]

[17]. Flohr TG, McCollough CH, Bruder H, et al. , First performance evaluation of a dual-source CT (DSCT) system [J], Eur. Radiol 16 (2) (2006) 256–268. [PubMed: 16341833]

[18]. Yu L, Leng S, McCollough CH, Dual-energy CT-based monochromatic imaging [J], AJR Am. J. Roentgenol 199 (5 Suppl) (2012) S9–S15. [PubMed: 23097173]

[19]. Graser A, Johnson TR, Chandarana H, et al. , Dual energy CT: preliminary observations and potential clinical applications in the abdomen [J], Eur. Radiol 19 (1) (2009) 13–23. [PubMed: 18677487]

[20]. Yanlan Liu KA, Lehui LU, Nanoparticulate X ray Computed Tomography Contrast Agents: From Design Validation to *in Vivo* Applications [J], Acc. Chem. Res 45(10) (2012) 1817–1827. [PubMed: 22950890]

[21]. Kruger RA, Riederer SJ, Mistretta CA, Relative properties of tomography, K-edge imaging, and K-edge tomography [J], Med. Phys 4 (3) (1977) 244–249. [PubMed: 329091]

[22]. Riederer SJ, Mistretta CA, Selective iodine imaging using K-edge energies in computerized x-ray tomography [J], Med. Phys 4 (6) (1977) 474–481. [PubMed: 927384]

[23]. Rutherford RA, Pullan BR, Isherwood I, X-Ray Energies for Effective Atomic Number Determination [J], Neuroradiology 11(1) (1976) 23–8. [PubMed: 934469]

[24]. Daniele Marin DTB, Mileto Achille, Nelson Rendon C., State of the Art: Dual-Energy CT of the Abdomen [J], Radiology 271 (2) (2014) 327–342. [PubMed: 24761954]

[25]. Johnson TRC, Krauß B, Sedlmair M, et al. , Material differentiation by dual energy CT: initial experience [J], Eur. Radiol 17 (6) (2006) 1510–1517. [PubMed: 17151859]

[26]. Coursey CA, R C N, Boll DT, Paulson EK, Ho LM, Neville AM, Marin D, Gupta RT, Schindera ST. Dual-Energy Multidetector CT: How Does It Work, What Can It Tell Us, and When Can We Use It in Abdominopelvic Imaging? [J], RadioGraphics, 30(4) (2010) 1037–1055. [PubMed: 20631367]

[27]. Boll Daniel T., N A P, Paulson Erik K., Merkle Elmar M., Nelson Rendon C., Schindera Sebastian T., Roessl Ewald, Martens Gerhard, Proksa Roland, Fleiter Thorsten R., Schlomka Jens-Peter, Focal Cystic High-Attenuation Lesions: Characterization in Renal Phantom by Using Photon-counting Spectral CT—Improved Differentiation of Lesion Composition [J], Radiology 254(1) (2010) 270–6. [PubMed: 20032158]

[28]. Primak AN, J C R G, Liu X, Yu L, Mccollough CH, Improved dual-energy material discrimination for dual-source CT by means of additional spectral filtration [J], Med Phys 36(4) (2009) 1359–1369. [PubMed: 19472643]

[29]. Alvarez RE, Macovski A, Energy-selective Reconstructions in X-ray Computerized Tomography [J], Phys. Med. Biol 21 (5) (1976) 733–744. [PubMed: 967922]

[30]. Sanghavi PS, Jankharia BG, Applications of dual energy CT in clinical practice: A pictorial essay [J], Indian J. Radiol. Imaging 29 (3) (2019) 289–298. [PubMed: 31741598]

[31]. Matsumoto K, M J, Tanami Y, Ueno A, Yamada M, Kuribayashi S, Virtual Monochromatic Spectral Imaging with Fast Kilovoltage Switching:Imporved Image Quality as Compared with That Obtained with Conventional 120-kVp CT [J], Radiology 259(1) (2011) 257–262. [PubMed: 21330561]

[32]. Schmidt B, Flohr T, Principles and applications of dual source CT [J], Phys. Med 79 (2020) 36–46. [PubMed: 33115699]

[33]. Petersilka M, Bruder H, Krauss B, et al. , Technical principles of dual source CT [J], Eur. J. Radiol 68 (3) (2008) 362–368. [PubMed: 18842371]

[34]. Johnson TR, Dual-energy CT: general principles [J], AJR Am. J. Roentgenol 199 (5 Suppl) (2012) S3–S8. [PubMed: 23097165]

[35]. Bamberg F, Dierks A, Nikolaou K, et al. , Metal artifact reduction by dual energy computed tomography using monoenergetic extrapolation [J], Eur. Radiol 21 (7) (2011) 1424–1429. [PubMed: 21249370]

[36]. Große Hokamp Nils, Maintz D, Shapira Nadav, Chang De-Hua, Noël Peter B., Technical background of a novel detector-based approach to dual-energy computed tomography [J], Diagn Interv Radiol 26 (1) (2020) 68–71. [PubMed: 31904573]

[37]. Hamid S, Nasir MU, So A, et al. , Clinical Applications of Dual-Energy CT [J], Korean J. Radiol 22 (6) (2021) 970–982. [PubMed: 33856133]

[38]. Fornaro J, Leschka S, Hibbeln D, et al. , Dual- and multi-energy CT: approach to functional imaging [J], Insights Imaging 2 (2) (2011) 149–159. [PubMed: 22347944]

[39]. Hsieh J, Flohr T, Computed tomography recent history and future perspectives [J], J. Med. Imaging (Bellingham) 8 (5) (2021) 052109. [PubMed: 34395720]

[40]. Flohr T, Petersilka M, Henning A, et al. , Photon-counting CT review [J], Phys. Med 79 (2020) 126–136. [PubMed: 33249223]

[41]. Willemink MJ, Persson M, Pourmorteza A, et al. , Photon-counting CT: Technical Principles and Clinical Prospects [J], Radiology 289 (2) (2018) 293–312. [PubMed: 30179101]

[42]. Cuccione E, Chhour P, Si-Mohamed S, et al. , Multicolor spectral photon counting CT monitors and quantifies therapeutic cells and their encapsulating scaffold in a model of brain damage [J], Nanotheranostics 4 (3) (2020) 129–141. [PubMed: 32483519]

[43]. Mi-Jin Kang CMP, Lee Chang-Hyun, Goo Jin Mo, Lee Hyun Ju, Dual-Energy CT: Clinical Applications in Various Pulmonary Diseases [J], RadioGraphics 30(3) (2010) 685–698. [PubMed: 20462988]

[44]. Aran S, Shaqdan KW, Abujudeh HH, Dual-energy computed tomography (DECT) in emergency radiology: basic principles, techniques, and limitations [J], Emerg. Radiol 21 (4) (2014) 391–405. [PubMed: 24676736]

[45]. Yu L, Christner JA, Leng S, et al. , Virtual monochromatic imaging in dual-source dual-energy CT: Radiation dose and image quality [J], Med. Phys 38(12) (2011) 6371–6379. [PubMed: 22149820]

[46]. Yu Lifeng, Primak AN, Liu Xin, Mccollough Cynthia H., Image quality optimization and evaluation of linearly mixed images in dual-source, dual-energy CT [J], Med. Phys 36 (3) (2009) 1019–1024. [PubMed: 19378762]

[47]. Holmes DR 3rd, Fletcher JG, Apel A, et al. , Evaluation of non-linear blending in dual-energy computed tomography [J], Eur. J. Radiol 68 (3) (2008) 409–413. [PubMed: 18990521]

[48]. Vernuccio F, Meyer M, Mileto A, et al. , Use of Dual-Energy Computed Tomography for Evaluation of Genitourinary Diseases [J], Urol. Clin. North Am 45 (3) (2018) 297–310. [PubMed: 30031456]

[49]. Goo HW, Goo JM, Dual-Energy CT: New Horizon in Medical Imaging [J], Kor. J Radiol 18 (4) (2017) 555–569.

[50]. Meier A, Wurnig M, Desbiolles L, et al. , Advanced virtual monoenergetic images: improving the contrast of dual-energy CT pulmonary angiography [J], Clin. Radiol 70 (11) (2015) 1244–1251. [PubMed: 26231468]

[51]. Rassouli N, Etesami M, Dhanantwari A, et al. , Detector-based spectral CT with a novel dual-layer technology: principles and applications [J], Insights Imaging 8 (6) (2017) 589–598. [PubMed: 28986761]

[52]. Delesalle MA, Pontana F, Duhamel A, Faivre JB, Flohr T, Tacelli N, Remy J, Remy-Jardin M, Spectral Optimization of Chest CT Angiography with Reduced Iodine Load: Experience in 80 Patients Evaluated with Dual-Source, Dual-Energy CT [J], Radiology 267 (1) (2013) 256–266. [PubMed: 23319663]

[53]. Yin Q, Zou X, Zai X, et al. , Pancreatic ductal adenocarcinoma and chronic mass-forming pancreatitis: Differentiation with dual-energy MDCT in spectral imaging mode [J], Eur. J. Radiol 84 (12) (2015) 2470–2476. [PubMed: 26481480]

[54]. Ming Li XZ, Li Jianying, Yang Yanli, Lu Chen, Xu Hua, Yu Bo, Xiao Li, Zhang Guozhen, Hua Yanqing, Dual-Energy Computed Tomography Imaging of Thyroid Nodule Specimens Comparison With Pathologic Findings [J], Invest Radiol 47(1) (2012) 58–64. [PubMed: 21788907]

[55]. Goodsitt Mitchell M., E G C, Larson Sandra C., Accuracies of the synthesized monochromatic CT numbers and effective atomic numbers obtained with a rapid kVp switching dual energy CT scanner [J], Med. Phys 38(4) (2011) 2222–2232. [PubMed: 21626956]

[56]. Lu Z, Wu S, Yan C, et al. , Clinical value of energy spectrum curves of dual-energy computer tomography may help to predict pathological grading of gastric adenocarcinoma [J], Transl. Cancer Res 10 (1) (2021) 1–9. [PubMed: 35116234]

[57]. Wisenbaugh ES, Paden RG, Silva AC, et al. , Dual-energy vs conventional computed tomography in determining stone composition [J], Urology 83 (6) (2014) 1243–1247. [PubMed: 24548708]

[58]. Mallinson Paul I., T M C, Mclaughlin Patrick D., Nicolaou SAVVAS, Munk Peter L., Ouellette Hugue A., Dual-Energy CT for the Musculoskeletal System [J], Radiology, 281(3) (2016) 690–707. [PubMed: 27870622]

[59]. Nicolaou S, Liang T, Murphy DT, et al. , Dual-energy CT: a promising new technique for assessment of the musculoskeletal system [J], AJR Am. J. Roentgenol 199 (5 Suppl) (2012) S78–S86. [PubMed: 23097171]

[60]. Nicolaou S, Yong-Hing CJ, Galea-Soler S, et al. , Dual-energy CT as a potential new diagnostic tool in the management of gout in the acute setting [J], AJR Am. J. Roentgenol 194 (4) (2010) 1072–1078. [PubMed: 20308513]

[61]. Sodickson AD, Keraliya A, Czakowski B, et al. , Dual energy CT in clinical routine: how it works and how it adds value [J], Emerg. Radiol 28 (1) (2021) 103–117. [PubMed: 32483665]

[62]. Glazebrook Katrina N., L S G, Murthy Naveen S., Black David F., Bongartz Tim, Manek Nisha J., Leng Shuai, Fletcher Joel G., Mccollough Cynthia H., Identification of Intraarticular and

Periarticular Uric Acid Crystals with Dual-Energy CT: Initial Evaluation [J]. Radiology, 261(2) (2011) 516–24. [PubMed: 21926378]

[63]. Primak AN, Fletcher JG, Vrtiska TJ, et al. , Noninvasive differentiation of uric acid versus non-uric acid kidney stones using dual-energy CT [J], Acad. Radiol 14 (12) (2007) 1441–1447. [PubMed: 18035274]

[64]. Liu Xin, Yu L, Primak Andrew N., Mccollough Cynthia H., Quantitative imaging of element composition and mass fraction using dual-energy CT: Three-material decomposition [J], Med. Phys 36 (5) (2009) 1602–1609. [PubMed: 19544776]

[65]. Graser Anno, T R C J, Bader Markus, Staehler Michael, Haseke Nicolas, Nikolaou Konstantin, Reiser Maximilian F., Stief Christian G., Becker Christoph R., Dual Energy CT Characterization of Urinary Calculi: Initial *In Vitro* and Clinical Experience [J], Invest. Radiol 43(2) (2008) 112–9. [PubMed: 18197063]

[66]. Choi HK, Al-Arfaj AM, Eftekhari A, et al. , Dual energy computed tomography in tophaceous gout [J], Ann. Rheum. Dis 68 (10) (2009) 1609–1612. [PubMed: 19066180]

[67]. Terkeltaub R, Update on gout: new therapeutic strategies and options [J], Nat. Rev. Rheumatol 6 (1) (2010) 30–38. [PubMed: 20046204]

[68]. Karcaaltincaba M, Aktas A, Dual-energy CT revisited with multidetector CT: review of principles and clinical applications [J], Diagn Interv. Radiol 17 (3) (2011) 181–194. [PubMed: 20945292]

[69]. Brockmann C, Jochum S, Sadick M, et al. , Dual-energy CT angiography in peripheral arterial occlusive disease [J], Cardiovasc. Intervent. Radiol 32 (4) (2009) 630–637. [PubMed: 19130122]

[70]. Lell M, Tomandl BF, Anders K, et al. , Computed tomography angiography versus digital subtraction angiography in vascular mapping for planning of microsurgical reconstruction of the mandible [J], Eur. Radiol 15 (8) (2005) 1514–1520. [PubMed: 15856243]

[71]. Muthusami P, Shkumat N, Rea V, et al. , CT reconstruction and MRI fusion of 3D rotational angiography in the evaluation of pediatric cerebrovascular lesions [J], Neuroradiology 59 (6) (2017) 625–633. [PubMed: 28349170]

[72]. Pratt P, Ives M, Lawton G, et al. , Through the HoloLens looking glass: augmented reality for extremity reconstruction surgery using 3D vascular models with perforating vessels [J], Eur Radiol Exp 2 (1) (2018) 2. [PubMed: 29708204]

[73]. Korn A, Bender B, Thomas C, et al. , Dual energy CTA of the carotid bifurcation: advantage of plaque subtraction for assessment of grade of the stenosis and morphology [J], Eur. J. Radiol 80 (2) (2011) E120–E125. [PubMed: 20833492]

[74]. Duan S, Lv S, Ye F, et al. , Imaging anatomy and variation of vertebral artery and bone structure at craniocervical junction [J], Eur. Spine J 18 (8) (2009) 1102–1108. [PubMed: 19288143]

[75]. Falchi M, Rollandi GA, CT of pelvic fractures [J], Eur. J. Radiol 50 (1) (2004) 96–105. [PubMed: 15093240]

[76]. Si-Mohamed S, Bar-Ness D, Sigovan M, et al. , Review of an initial experience with an experimental spectral photon-counting computed tomography system [J], Nucl. Instrum. Methods Phys. Res., Sect. A 873 (2017) 27–35.

[77]. Yeh BM, Fitzgerald PF, Edic PM, et al. , Opportunities for new CT contrast agents to maximize the diagnostic potential of emerging spectral CT technologies [J], Adv. Drug Deliv. Rev 113 (2017) 201–222. [PubMed: 27620496]

[78]. Hasebroock KM, Serkova NJ, Toxicity of MRI and CT contrast agents [J], Expert Opin. Drug Metab. Toxicol 5 (4) (2009) 403–416. [PubMed: 19368492]

[79]. Oliva MR, Erturk SM, Ichikawa T, et al. , Gastrointestinal Tract Wall Visualization and distention during abdominal and pelvic multidetector CT with a neutral barium sulphate suspension: comparison with positive barium sulphate suspension and with water [J], JBR-BTR 95 (4) (2012) 237–242. [PubMed: 23019990]

[80]. Al-Buriahi MS, Tonguc BT, Mass attenuation coefficients, effective atomic numbers and electron densities of some contrast agents for computed tomography [J], Radiat. Phys. Chem 166 (2020).

[81]. Achenbach S, Paul JF, Laurent F, et al. , Comparative assessment of image quality for coronary CT angiography with iobitridol and two contrast agents with higher iodine concentrations:

iopromide and iomeprol. A multicentre randomized double-blind trial [J], Eur. Radiol 27 (2) (2017) 821–830. [PubMed: 27271922]

[82]. Rogers D, Sheth C, Eisenmenger L, et al. , Iopamidol as an oral contrast media for computed tomography: a taste comparison to iohexol, diatrizoate sodium, and barium sulfate [J], Abdom Radiol (NY) 42 (12) (2017) 2822–2826. [PubMed: 28669111]

[83]. Ding Y, Zhang X, Xu Y, et al. , Polymerization-induced self-assembly of large-scale iohexol nanoparticles as contrast agents for X-ray computed tomography imaging [J], Polym. Chem 9 (21) (2018) 2926–2935.

[84]. Wang Carolyn L., R H C Ellis James H., Adusumilli Saroja, Dunnick N. Reed, Frequency, Management, and Outcome of Extravasation of Nonionic Iodinated Contrast Medium in 69 657 Intravenous Injections [J]. Radiology 243(1) (2007) 80–7. [PubMed: 17392249]

[85]. Namasivayam S, Kalra MK, Torres WE, et al. , Adverse reactions to intravenous iodinated contrast media: an update [J], Curr. Probl. Diagn. Radiol 35 (4) (2006) 164–169. [PubMed: 16814003]

[86]. Hahn MA, Singh AK, Sharma P, et al. , Nanoparticles as contrast agents for in-vivo bioimaging: current status and future perspectives [J], Anal. Bioanal. Chem 399 (1) (2011) 3–27. [PubMed: 20924568]

[87]. Xue X, Qu H, Li Y, Stimuli-responsive crosslinked nanomedicine for cancer treatment [J], Exploration (2022).

[88]. Xie J, Lee S, Chen X, Nanoparticle-based theranostic agents [J], Adv. Drug Deliv. Rev 62 (11) (2010) 1064–1079. [PubMed: 20691229]

[89]. Lee DE, Koo H, Sun IC, et al. , Multifunctional nanoparticles for multimodal imaging and theragnosis [J], Chem. Soc. Rev 41 (7) (2012) 2656–2672. [PubMed: 22189429]

[90]. Lee N, Choi SH, Hyeon T, Nano-sized CT contrast agents [J], Adv. Mater 25(19) (2013) 2641–2660. [PubMed: 23553799]

[91]. Zhao Y, Zhang Z, Pan Z, et al. , Advanced bioactive nanomaterials for biomedical applications [J], Exploration 1 (3) (2021).

[92]. Price EW, Orvig C, Matching chelators to radiometals for radiopharmaceuticals [J], Chem. Soc. Rev 43 (1) (2014) 260–290. [PubMed: 24173525]

[93]. Hofman MS, Violet J, Hicks RJ, et al. , [177Lu]-PSMA-617 radionuclide treatment in patients with metastatic castration-resistant prostate cancer (LuPSMA trial): a single-centre, single-arm, phase 2 study [J, Lancet Oncol. 19(6) (2018) 825–833. [PubMed: 29752180]

[94]. Zhou J, Zhu X, Chen M, et al. , Water-stable NaLuF$_4$-based upconversion nanophosphors with long-term validity for multimodal lymphatic imaging [J], Biomaterials 33 (26) (2012) 6201–6210. [PubMed: 22717364]

[95]. Kulkarni HR, Singh A, Schuchardt C, et al. , PSMA-Based Radioligand Therapy for Metastatic Castration-Resistant Prostate Cancer: The Bad Berka Experience Since 2013 [J], J. Nucl. Med 57 (Suppl 3) (2016) 97S–104S. [PubMed: 27694180]

[96]. Wang Xiaolan D M, Taguchi Katsuyuki, Wagenaar Douglas J., Patt Bradley E., Frey Eric C., Material separation in x-ray CT with energy resolved photon-counting detectors [J], Med Phys, (2011) 7961.

[97]. Singh J, Daftary A, Iodinated contrast media and their adverse reactions [J], J. Nucl. Med. Technol 36(2) (2008) 69–74; quiz 6–7. [PubMed: 18483141]

[98]. Jost G, Lengsfeld P, Lenhard DC, et al. , Viscosity of iodinated contrast agents during renal excretion [J], Eur. J. Radiol 80 (2) (2011) 373–377. [PubMed: 21376497]

[99]. Morcos SK, H S T, Webb JAW, Members of the contrast media safety committee of the european society of urogenital radiology (ESUR), Contrast-media-induced nephrotoxicity: a consensus report [J], Eur. Radiol 9(8) (1999) 1602–13. [PubMed: 10525875]

[100]. Hsu JC, Nieves LM, Betzer O, et al. , Nanoparticle contrast agents for X-ray imaging applications [J], Wiley Interdiscip. Rev. Nanomed. Nanobiotechnol 12 (6) (2020) e1642. [PubMed: 32441050]

[101]. Allphin AJ, Mowery YM, Lafata KJ, et al. , Photon Counting CT and Radiomic Analysis Enables Differentiation of Tumors Based on Lymphocyte Burden [J], Tomography 8 (2) (2022) 740–753. [PubMed: 35314638]

[102]. de Vries A, Custers E, Lub J, et al. , Block-copolymer-stabilized iodinated emulsions for use as CT contrast agents [J], Biomaterials 31 (25) (2010) 6537–6544. [PubMed: 20541800]

[103]. Attia MF, Anton N, Chiper M, et al. , Biodistribution of X-Ray Iodinated Contrast Agent in Nano-Emulsions Is Controlled by the Chemical Nature of the Oily Core [J], ACS Nano 8 (10) (2014) 10537–10550. [PubMed: 25284066]

[104]. Vladimir P Torchilin D, Frank-Kamenetsky Maria D., Wolf Gerald L., CT Visualization of Blood Pool in Rats by Using Long-circulating, Iodine-containing Micelles [J], Acad, Radiol, 6(1) (1999) 61–5. [PubMed: 9891154]

[105]. Jin E, Lu ZR, Biodegradable iodinated polydisulfides as contrast agents for CT angiography [J], Biomaterials 35 (22) (2014) 5822–5829. [PubMed: 24768156]

[106]. Dekrafft KE, Xie Z, Cao G, et al. , Iodinated nanoscale coordination polymers as potential contrast agents for computed tomography [J], Angew. Chem. Int. Ed. Engl 48 (52) (2009) 9901–9904. [PubMed: 19937883]

[107]. Hallouard F, Anton N, Choquet P, et al. , Iodinated blood pool contrast media for preclinical X-ray imaging applications–a review [J], Biomaterials 31 (24) (2010) 6249–6268. [PubMed: 20510444]

[108]. Stacul F, van der Molen AJ, Reimer P, et al. , Contrast induced nephropathy: updated ESUR Contrast Media Safety Committee guidelines [J], Eur. Radiol 21(12) (2011) 2527–2541. [PubMed: 21866433]

[109]. Zhang X, Dai Z, Advances in multifunctional nano-sized CT contrast agents [J], Chin. Sci. Bull 60 (35) (2015) 3424–3437.

[110]. Haller C, Hizoh I, The cytotoxicity of iodinated radiocontrast agents on renal cells *in vitro* [J], Invest. Radiol 39 (3) (2004) 149–154. [PubMed: 15076007]

[111]. Bourin M, Jolliet P, Ballereau F, An Overview of the Clinical Pharmacokinetics of X-Ray Contrast Media [J], Biomaterials (1997).

[112]. Shilo M, Reuveni T, Motiei M, et al. , Nanoparticles as computed tomography contrast agents: current status and future perspectives [J], Nanomedicine 7(2) (2012) 257–269. [PubMed: 22339135]

[113]. Annapragada Ananth V., E H, Divekar Abhay, Karathanasis Efstathios, Ghaghada Ketan B., High-Resolution CT Vascular Imaging Using Blood Pool Contrast Agents [J], Method. Debakey Cardiovascul. J 8(1) (2012) 18–22.

[114]. Balegamire J, Vandamme M, Chereul E, et al. , Iodinated polymer nanoparticles as contrast agent for spectral photon counting computed tomography [J], Biomater. Sci 8 (20) (2020) 5715–5728. [PubMed: 32935704]

[115]. Dean PB, Kivisaari L, Kormano Martti, Contrast Enhancement Pharmacokinetics of Six Ionic and Nonionic Contrast Media [J], Invest. Radiol 18 (4) (1983) 368–374. [PubMed: 6618828]

[116]. Pomerantz Stuart R., M S K, Zhang M.D. Da, Gupta PHDRAJIV, Rapalino P.H.D., MD Otto, Sahani MD Dushyant V., Lev MD Michael H., Virtual Monochromatic Reconstruction of Dual-energy Unenhanced Head CT at 65–75 keV Maximizes Image Quality Compared with Conventional Polychromatic CT [J], Radiology 266(1) (2013) 318–325. [PubMed: 23074259]

[117]. Zwicker C, M H, Langer R, Computed tomography with iodine-free contrast media [J], Eur. Radiol 7(7) (1997) 1123–6. [PubMed: 9265688]

[118]. Cardiovascular Division, D.O.M. Brigham, Women's Hospital, and harvard medical school, boston, Inflammation in atherosclerosis [J], Nature 420(6917) (2002) 868–74 [PubMed: 12490960]

[119]. H.G.K., InflammationAtherosclerosis, and Coronary Artery Disease [J], N. Engl. J. Med 353 (4) (2005) 429-.

[120]. Ross R, The pathogenesis of atherosclerosis: a perspective for the 1990s [J], Nature 362 (6423) (1993) 801–809. [PubMed: 8479518]

[121]. Ross R, Atherosclerosis-An Inflammatory Disease [J], New Engl. J. Med 340(2) (1999) 115–126. [PubMed: 9887164]

[122]. Libby P, Buring JE, Badimon L, et al. , Atherosclerosis [J], Nat. Rev. Dis. Primers 5 (1) (2019) 56. [PubMed: 31420554]

[123]. Pan D, Schirra CO, Senpan A, et al. , An Early Investigation of Ytterbium Nanocolloids for Selective and Quantitative "Multicolor" Spectral CT Imaging [J], ACS Nano 6 (4) (2012) 3364–3370. [PubMed: 22385324]

[124]. Lew DP, Waldvogel FA, Osteomyelitis [J], The Lancet 364 (9431) (2004) 369–379.

[125]. Wang Y, Jiang C, He W, et al. , Targeted Imaging of Damaged Bone *in Vivo* with Gemstone Spectral Computed Tomography [J], ACS Nano 10 (4) (2016) 4164–4172. [PubMed: 27043072]

[126]. Liu M, Shi Z, Wang X, et al. , Simultaneous enhancement of red upconversion luminescence and CT contrast of NaGdF4:Yb, Er nanoparticles via L^{u3}+ doping [J], Nanoscale 10 (43) (2018) 20279–20288. [PubMed: 30371720]

[127]. Sun Y, Peng J, Feng W, et al. , Upconversion nanophosphors Naluf(4):Yb, Tm for lymphatic imaging in vivo by real-time upconversion luminescence imaging under ambient light and high-resolution X-ray CT [J], Theranostics 3(5) (2013) 346–353. [PubMed: 23650481]

[128]. Sadykova LR, Ntekim AI, Muyangwa-Semenova M, et al. , Epidemiology and Risk Factors of Osteosarcoma [J], Cancer Invest. 38 (5) (2020) 259–269. [PubMed: 32400205]

[129]. Jin Y, Ni D, Gao L, et al. , Harness the Power of Upconversion Nanoparticles for Spectral Computed Tomography Diagnosis of Osteosarcoma [J], Adv. Funct. Mater 28 (33) (2018).

[130]. Kim J, Bar-Ness D, Si-Mohamed S, et al. , Assessment of candidate elements for development of spectral photon-counting CT specific contrast agents [J], Sci. Rep 8 (1) (2018) 12119. [PubMed: 30108247]

[131]. Nowak T, Hupfer M, Brauweiler R, et al. , Potential of high-Z contrast agents in clinical contrast-enhanced computed tomography [J], Med. Phys 38 (12) (2011) 6469–6482. [PubMed: 22149830]

[132]. Ostadhossein F, Tripathi I, Benig L, et al. , Multi-"Color" Delineation of Bone Microdamages Using Ligand-Directed Sub-5 nm Hafnia Nanodots and Photon Counting CT Imaging [J], Adv. Funct. Mater 30 (4) (2019).

[133]. Ostadhossein F, Moitra P, Gunaseelan N, et al. , Hitchhiking probiotic vectors to deliver ultra-small hafnia nanoparticles for 'Color' gastrointestinal tract photon counting X-ray imaging [J], Nanoscale Horiz. 7 (5) (2022) 533–542. [PubMed: 35311837]

[134]. Rathnayake S, Mongan J, Torres AS, et al. , In vivo comparison of tantalum, tungsten, and bismuth enteric contrast agents to complement intravenous iodine for double-contrast dual-energy CT of the bowel [J], Contrast Media Mol. Imaging 11 (4) (2016) 254–261. [PubMed: 26892945]

[135]. Oh MH, Lee N, Kim H, et al. , Large-scale synthesis of bioinert tantalum oxide nanoparticles for X-ray computed tomography imaging and bimodal image-guided sentinel lymph node mapping [J], J. Am. Chem. Soc 133 (14) (2011) 5508–5515. [PubMed: 21428437]

[136]. Bonitatibus PJ Jr., Torres AS, Goddard GD, et al. , Synthesis, characterization, and computed tomography imaging of a tantalum oxide nanoparticle imaging agent [J], Chem. Commun. (Camb.) 46 (47) (2010) 8956–8958. [PubMed: 20976321]

[137]. Lambert JW, Sun Y, Stillson C, et al. , An Intravascular Tantalum Oxide-based CT Contrast Agent: Preclinical Evaluation Emulating Overweight and Obese Patient Size [J], Radiology 289 (1) (2018) 103–110. [PubMed: 29969071]

[138]. Dong K, Liu Z, Liu J, et al. , Biocompatible and high-performance amino acids-capped MnWO4 nanocasting as a novel non-lanthanide contrast agent for X-ray computed tomography and T(1)-weighted magnetic resonance imaging [J], Nanoscale 6 (4) (2014) 2211–2217. [PubMed: 24382605]

[139]. Liu J, Han J, Kang Z, et al. , In vivo near-infrared photothermal therapy and computed tomography imaging of cancer cells using novel tungsten-based theranostic probe [J], Nanoscale 6 (11) (2014) 5770–5776. [PubMed: 24736832]

[140]. Mongan JR, Fu S,YJ, Wang RT, Jone EF, Gao DW; Yeh BM, In Vivo Differentiation of Complementary Contrast Media at Dual-Energy CT [J], Radiology 265(1) (2012) 267–72. [PubMed: 22778447]

[141]. Shen S, Chao Y, Dong Z, et al. , Bottom-Up Preparation of Uniform Ultrathin Rhenium Disulfide Nanosheets for Image-Guided Photothermal Radiotherapy [J], Adv. Funct. Mater 27 (28) (2017).

[142]. Miao ZH, Lv LX, Li K, et al. , Liquid Exfoliation of Colloidal Rhenium Disulfide Nanosheets as a Multifunctional Theranostic Agent for *In Vivo* Photoacoustic/CT Imaging and Photothermal Therapy [J], Small 14 (14) (2018) e1703789. [PubMed: 29468828]

[143]. Wang X, Wang J, Pan J, et al. , Rhenium Sulfide Nanoparticles as a Biosafe Spectral CT Contrast Agent for Gastrointestinal Tract Imaging and Tumor Theranostics *in Vivo* [J], ACS Appl. Mater. Interfaces 11 (37) (2019) 33650–33658. [PubMed: 31448891]

[144]. Yu Junfeng YD, Xiaofeng Min, Zili Guo, Jiong Zhang, Yongxian Wang, Knapp FF JR, [188Re]Rhenium Sulfide Suspension: A Potential Radiopharmaceutical for Tumor Treatment Following Intra-Tumor Injection [J], Nucl. Med. Biol 26(5) (1999) 573–9. [PubMed: 10473197]

[145]. Yu Junfeng YD, Xxiaofeng Min, Zili Guo, Jiong Zhang, Yongxian Wang, Knapp FF JR, Preparation of [188Re] Rhenium Sulfide Suspension and Its Biodistribution Following Intra-Tumor Injection in Mice [J], J. Labell. Comp. Radiopharm 3, 42(3) (1999) 233–43.

[146]. Junfeng Yu, Ruping Z, Xinlan Dai, Xiaofeng Min, Jianying Xu, Weiqing Hu, Duanzhi Yin, Wei Zhou, Hong Xie, Yongxian Wang, Knapp FF Jr., Intratumoral Injection with [188Re]Rhenium Sulfide Suspension for Treatment of Transplanted Human Liver Carcinoma in Nude Mice [J], Nucl. Med. Biol 27(4) (2000) 347–352. [PubMed: 10938468]

[147]. Frager David, Medwid SW, Baer Jeanne W., Mollinelli Bruce, Friedman Marvin, CT of Small-Bowel Obstruction: Value in Establishing the Diagnosis and Determining the Degree and Cause [J], AJR Am. J. Roentgenol 162 (1) (1994) 37–41. [PubMed: 8273686]

[148]. Zhang Y, Qian J, Wang D, et al. , Multifunctional gold nanorods with ultrahigh stability and tunability for *in vivo* fluorescence imaging, SERS detection, and photodynamic therapy [J], Angew. Chem. Int. Ed. Engl 52 (4) (2013) 1148–1151. [PubMed: 23233455]

[149]. Youssef AM, Abdel-Aziz MS, El-Sayed SM, Chitosan nanocomposite films based on Ag-NP and Au-NP biosynthesis by Bacillus Subtilis as packaging materials [J], Int. J. Biol. Macromol 69 (2014) 185–191. [PubMed: 24875320]

[150]. Yin D, Li X, Ma Y, et al. , Targeted cancer imaging and photothermal therapy *via* monosaccharide-imprinted gold nanorods [J], Chem. Commun. (Camb.) 53 (50) (2017) 6716–6719. [PubMed: 28585650]

[151]. Peng C, Zheng L, Chen Q, et al. , PEGylated dendrimer-entrapped gold nanoparticles for *in vivo* blood pool and tumor imaging by computed tomography [J], Biomaterials 33 (4) (2012) 1107–1119. [PubMed: 22061490]

[152]. Connor EE, Mwamuka J, Gole A, et al. , Gold nanoparticles are taken up by human cells but do not cause acute cytotoxicity [J], Small 1 (3) (2005) 325–327. [PubMed: 17193451]

[153]. Guo J, Rahme K, He Y, et al. , Gold nanoparticles enlighten the future of cancer theranostics [J], Int. J. Nanomed 12 (2017) 6131–6152.

[154]. Bouche M, Hsu JC, Dong YC, et al. , Recent Advances in Molecular Imaging with Gold Nanoparticles [J], Bioconjug. Chem 31 (2) (2020) 303–314. [PubMed: 31682405]

[155]. Clark DP, Ghaghada K, Moding EJ, et al. , *In vivo* characterization of tumor vasculature using iodine and gold nanoparticles and dual energy micro-CT [J], Phys. Med. Biol 58 (6) (2013) 1683–1704. [PubMed: 23422321]

[156]. Libutti SK, Paciotti GF, Byrnes AA, et al. , Phase I and pharmacokinetic studies of CYT-6091, a novel PEGylated colloidal gold-rhTNF nanomedicine [J], Clin. Cancer Res 16 (24) (2010) 6139–6149. [PubMed: 20876255]

[157]. Moghiseh M, Lowe C, Lewis JG, et al. , Spectral Photon-Counting Molecular Imaging for Quantification of Monoclonal Antibody-Conjugated Gold Nanoparticles Targeted to Lymphoma and Breast Cancer: An In Vitro Study [J], Contrast Media Mol. Imaging 2018 (2018) 2136840. [PubMed: 30662379]

[158]. Cormode DP, Roessl E, Thran A, et al. , Atherosclerotic Plaque Composition: Analysis with Multicolor CT and Targeted Gold Nanoparticles [J], Radiology 256 (3) (2010) 774–782. [PubMed: 20668118]

[159]. Si-Mohamed SA, Sigovan M, Hsu JC, et al. , In Vivo Molecular K-Edge Imaging of Atherosclerotic Plaque Using Photon-counting CT [J], Radiology 300 (1) (2021) 98–107. [PubMed: 33944628]

[160]. Si-Mohamed S, Bar-Ness D, Sigovan M, et al. , Multicolour imaging with spectral photon-counting CT: a phantom study [J], Eur. Radiol. Exp 2 (1) (2018) 34. [PubMed: 30327898]

[161]. Cormode DP, Si-Mohamed S, Bar-Ness D, et al. , Multicolor spectral photon-counting computed tomography: in vivo dual contrast imaging with a high count rate scanner [J], Sci. Rep 7 (1) (2017) 4784. [PubMed: 28684756]

[162]. Symons R, Krauss B, Sahbaee P, et al. , Photon-counting CT for simultaneous imaging of multiple contrast agents in the abdomen: An in vivo study [J], Med. Phys 44 (10) (2017) 5120–5127. [PubMed: 28444761]

[163]. Si-Mohamed S, Thivolet A, Bonnot PE, et al. , Improved Peritoneal Cavity and Abdominal Organ Imaging Using a Biphasic Contrast Agent Protocol and Spectral Photon Counting Computed Tomography K-Edge Imaging [J], Invest. Radiol 53 (10) (2018) 629–639. [PubMed: 29794948]

[164]. Symons R, Cork TE, Lakshmanan MN, et al. , Dual-contrast agent photon-counting computed tomography of the heart: initial experience [J], Int. J. Cardiovasc. Imaging 33 (8) (2017) 1253–1261. [PubMed: 28289990]

[165]. Baer K, Kieser S, Schon B, et al. , Spectral CT imaging of human osteoarthritic cartilage via quantitative assessment of glycosaminoglycan content using multiple contrast agents [J], APL Bioeng. 5 (2) (2021) 026101. [PubMed: 33834156]

[166]. Anderson NG, Butler AP, Clinical applications of spectral molecular imaging: potential and challenges [J], Contrast Media Mol. Imaging 9 (1) (2014) 3–12. [PubMed: 24470290]

[167]. Wei B, Zhang X, Zhang C, et al. , Facile Synthesis of Uniform-Sized Bismuth Nanoparticles for CT Visualization of Gastrointestinal Tract in Vivo [J], ACS Appl. Mater. Interfaces 8 (20) (2016) 12720–12726. [PubMed: 27144639]

[168]. Li Z, Hu Y, Miao Z, et al. , Dual-Stimuli Responsive Bismuth Nanoraspberries for Multimodal Imaging and Combined Cancer Therapy [J], Nano Lett. 18 (11) (2018) 6778–6788. [PubMed: 30288978]

[169]. Hu X, Sun J, Li F, et al. , Renal-Clearable Hollow Bismuth Subcarbonate Nanotubes for Tumor Targeted Computed Tomography Imaging and Chemoradiotherapy [J], Nano Lett. 18 (2) (2018) 1196–1204. [PubMed: 29297694]

[170]. Liao W, Lei P, Pan J, et al. , Bi-DTPA as a high-performance CT contrast agent for in vivo imaging [J], Biomaterials 203 (2019) 1–11. [PubMed: 30844678]

[171]. Li Z, Liu J, Hu Y, et al. , Biocompatible PEGylated bismuth nanocrystals: "All-in-one" theranostic agent with triple-modal imaging and efficient in vivo photothermal ablation of tumors [J], Biomaterials 141 (2017) 284–295. [PubMed: 28709019]

[172]. Yu N, Wang Z, Zhang J, et al. , Thiol-capped Bi nanoparticles as stable and all-in-one type theranostic nanoagents for tumor imaging and thermoradiotherapy [J], Biomaterials 161 (2018) 279–291. [PubMed: 29425848]

[173]. Lei P, An R, Zhang P, et al. , Ultrafast Synthesis of Ultrasmall Poly (Vinylpyrrolidone)-Protected Bismuth Nanodots as a Multifunctional Theranostic Agent for In Vivo Dual-Modal CT/Photothermal-Imaging-Guided Photothermal Therapy [J], Adv. Funct. Mater 27 (35) (2017).

[174]. Wu B, Lu ST, Yu H, et al. , Gadolinium-chelate functionalized bismuth nanotheranostic agent for in vivo MRI/CT/PAI imaging-guided photothermal cancer therapy [J], Biomaterials 159 (2018) 37–47. [PubMed: 29309992]

[175]. Bi H, He F, Dong Y, et al. , Bismuth Nanoparticles with "Light" Property Served as a Multifunctional Probe for X-ray Computed Tomography and Fluorescence Imaging [J], Chem. Mater 30 (10) (2018) 3301–3307.

[176]. Li L, Lu Y, Jiang C, et al. , Actively Targeted Deep Tissue Imaging and Photothermal-Chemo Therapy of Breast Cancer by Antibody-Functionalized Drug-Loaded X-Ray-Responsive Bismuth Sulfide@Mesoporous Silica Core-Shell Nanoparticles [J], Adv. Funct. Mater 28 (5) (2018).

[177]. Guo Z, Zhu S, Yong Y, et al. , Synthesis of BSA-Coated BiOI@Bi$_2$S$_3$ Semiconductor Heterojunction Nanoparticles and Their Applications for Radio/Photodynamic/Photothermal Synergistic Therapy of Tumor [J], Adv. Mater 29 (44) (2017).

[178]. Cheng Y, Chang Y, Feng Y, et al. , Bismuth Sulfide Nanorods with Retractable Zinc Protoporphyrin Molecules for Suppressing Innate Antioxidant Defense System and

Strengthening Phototherapeutic Effects [J], Adv. Mater 31 (10) (2019) e1806808. [PubMed: 30633400]

[179]. Lu Y, Li L, Lin Z, et al. , Enhancing Osteosarcoma Killing and CT Imaging Using Ultrahigh Drug Loading and NIR-Responsive Bismuth Sulfide@Mesoporous Silica Nanoparticles [J], Adv. Healthc. Mater 7 (19) (2018) e1800602. [PubMed: 30102469]

[180]. Xiong Y, Sun F, Liu P, et al. , A biomimetic one-pot synthesis of versatile Bi_2S_3/FeS_2 theranostic nanohybrids for tumor-targeted photothermal therapy guided by CT/MR dual-modal imaging [J], Chem. Eng. J 378 (2019).

[181]. Ouyang R, Cao P, Jia P, et al. , Bistratal $Au@Bi_2S_3$ nanobones for excellent NIR-triggered/ multimodal imaging-guided synergistic therapy for liver cancer [J], Bioact. Mater 6 (2) (2021) 386–403. [PubMed: 32954056]

[182]. Rabin O, Manuel Perez J, Grimm J, et al. , An X-ray computed tomography imaging agent based on long-circulating bismuth sulphide nanoparticles [J], Nat. Mater 5 (2) (2006) 118–122. [PubMed: 16444262]

[183]. Liu Jing, Zhen X, Yan Liang, Zhou Liangjun, Tian Gan, Yin Wenyan, Wang Liming, Liu Ying, Hu Zhongbo, Gu Zhanjun, Chen Chunying, Zhao Yuliang, Bismuth Sulfide Nanorods as a Precision Nanomedicine for *in Vivo* Multimodal Imaging-Guided Photothermal Therapy of Tumor [J], ACS Nano 9 (1) (2015) 696–707. [PubMed: 25561009]

[184]. Wang Y, Zhao J, Chen Z, et al. , Construct of $MoSe_2/Bi_2Se_3$ nanoheterostructure: Multimodal CT/PT imaging-guided PTT/PDT/chemotherapy for cancer treating [J], Biomaterials 217 (2019) 119282. [PubMed: 31260884]

[185]. Yang C, Chang M, Yuan M, et al. , NIR-Triggered Multi-Mode Antitumor Therapy Based on Bi_2Se_3/Au Heterostructure with Enhanced Efficacy [J], Small 17 (28) (2021) e2100961. [PubMed: 34110686]

[186]. Li Z, Hu Y, Howard KA, et al. , Multifunctional Bismuth Selenide Nanocomposites for Antitumor Thermo-Chemotherapy and Imaging [J], ACS Nano 10 (1) (2016) 984–997. [PubMed: 26655250]

[187]. Li Z, Liu J, Hu Y, et al. , Multimodal Imaging-Guided Antitumor Photothermal Therapy and Drug Delivery Using Bismuth Selenide Spherical Sponge [J], ACS Nano 10 (10) (2016) 9646–9658. [PubMed: 27689234]

[188]. Mao F, Wen L, Sun C, et al. , Ultrasmall Biocompatible Bi_2Se_3 Nanodots for Multimodal Imaging-Guided Synergistic Radiophotothermal Therapy against Cancer [J], ACS Nano 10 (12) (2016) 11145–11155. [PubMed: 28024338]

[189]. Chen X, Wang R, Liu D, et al. , Prussian Blue Analogue Islands on BiOCl-Se Nanosheets for MR/CT Imaging-Guided Photothermal/Photodynamic Cancer Therapy [J], ACS Appl. Bio Mater 2 (3) (2019) 1213–1224.

[190]. Wang Y, Wu Y, Liu Y, et al. , BSA-Mediated Synthesis of Bismuth Sulfide Nanotheranostic Agents for Tumor Multimodal Imaging and Thermoradiotherapy [J], Adv. Funct. Mater 26 (29) (2016) 5335–5344.

[191]. Shahbazi MA, Faghfouri L, Ferreira MPA, et al. , The versatile biomedical applications of bismuth-based nanoparticles and composites: therapeutic, diagnostic, biosensing, and regenerative properties [J], Chem. Soc. Rev 49 (4) (2020) 1253–1321. [PubMed: 31998912]

[192]. Jakhmola A, Anton N, Vandamme TF, Inorganic nanoparticles based contrast agents for X-ray computed tomography [J], Adv. Healthc Mater 1(4) (2012) 413–431. [PubMed: 23184772]

[193]. Mohan R, Green bismuth [J], Nat. Chem 2 (4) (2010) 336. [PubMed: 21124518]

[194]. Bataller R, Brenner DA, Liver fibrosis [J], J Clin Invest 115 (2) (2005) 209–218. [PubMed: 15690074]

[195]. Pellicoro A, Ramachandran P, Iredale JP, et al. , Liver fibrosis and repair: immune regulation of wound healing in a solid organ [J], Nat. Rev. Immunol 14 (3) (2014) 181–194. [PubMed: 24566915]

[196]. Schuppan D, Kim YO, Evolving therapies for liver fibrosis [J], J Clin Invest 123 (5) (2013) 1887–1901. [PubMed: 23635787]

[197]. Seki E, Schwabe RF, Hepatic inflammation and fibrosis: functional links and key pathways [J], Hepatology 61 (3) (2015) 1066–1079. [PubMed: 25066777]

[198]. Jian ZC, Long JF, Liu YJ, et al. , Diagnostic value of two dimensional shear wave elastography combined with texture analysis in early liver fibrosis [J], World J. Clin. Cases 7 (10) (2019) 1122–1132. [PubMed: 31183343]

[199]. Ge M, Liu H, Zhang Y, et al. , The anti-hepatic fibrosis effects of dihydrotanshinone I are mediated by disrupting the yes-associated protein and transcriptional enhancer factor D2 complex and stimulating autophagy [J], Br. J. Pharmacol 174 (10) (2017) 1147–1160. [PubMed: 28257144]

[200]. Lurie Y, Webb M, Cytter-Kuint R, et al. , Non-invasive diagnosis of liver fibrosis and cirrhosis [J], World J. Gastroenterol 21 (41) (2015) 11567–11583. [PubMed: 26556987]

[201]. Zhang K, Han Y, Hu Z, et al. , SCARNA10, a nuclear-retained long non-coding RNA, promotes liver fibrosis and serves as a potential biomarker [J], Theranostics 9 (12) (2019) 3622–3638. [PubMed: 31281502]

[202]. Wu S, Meng X, Jiang X, et al. , Harnessing X-Ray Energy-Dependent Attenuation of Bismuth-Based Nanoprobes for Accurate Diagnosis of Liver Fibrosis [J], Adv. Sci. (Weinh) 8 (11) (2021) e2002548. [PubMed: 34105274]

[203]. Pan D, Roessl E, Schlomka JP, et al. , Computed tomography in color: NanoK-enhanced spectral CT molecular imaging [J], Angew. Chem. Int. Ed. Engl 49(50) (2010) 9635–9639. [PubMed: 21077082]

[204]. Adam SZ, Rabinowich A, Kessner R, et al. , Spectral CT of the abdomen: Where are we now? [J], Insights Imaging 12 (1) (2021) 138. [PubMed: 34580788]

[205]. Fitzgerald Paul F., R E C, Edic Peter M., Lambert Jack W., Torres Andrew S., Bonitatibus Peter J., Yeh Benjamin M.. CT Image Contrast of High-Z Elements: Phantom Imaging Studies and Clinical Implications [J], Radiology 278(3) (2015) 723–33. [PubMed: 26356064]

[206]. Ni D, Bu W, Ehlerding EB, et al. , Engineering of inorganic nanoparticles as magnetic resonance imaging contrast agents [J], Chem. Soc. Rev 46 (23) (2017) 7438–7468. [PubMed: 29071327]

[207]. Wang Q, Liang Z, Li F, et al. , Dynamically switchable magnetic resonance imaging contrast agents [J], Exploration 1 (2) (2021).

[208]. Cui X, Zhang Z, Yang Y, et al. , Organic radical materials in biomedical applications: State of the art and perspectives [J], Exploration 2 (2) (2022).

[209]. Debbage P, Jaschke W, Molecular imaging with nanoparticles: giant roles for dwarf actors [J], Histochem. Cell Biol 130 (5) (2008) 845–875. [PubMed: 18825403]

[210]. Schirra CO, Brendel B, Anastasio MA, et al. , Spectral CT: a technology primer for contrast agent development [J], Contrast Media Mol. Imaging 9 (1) (2014) 62–70. [PubMed: 24470295]
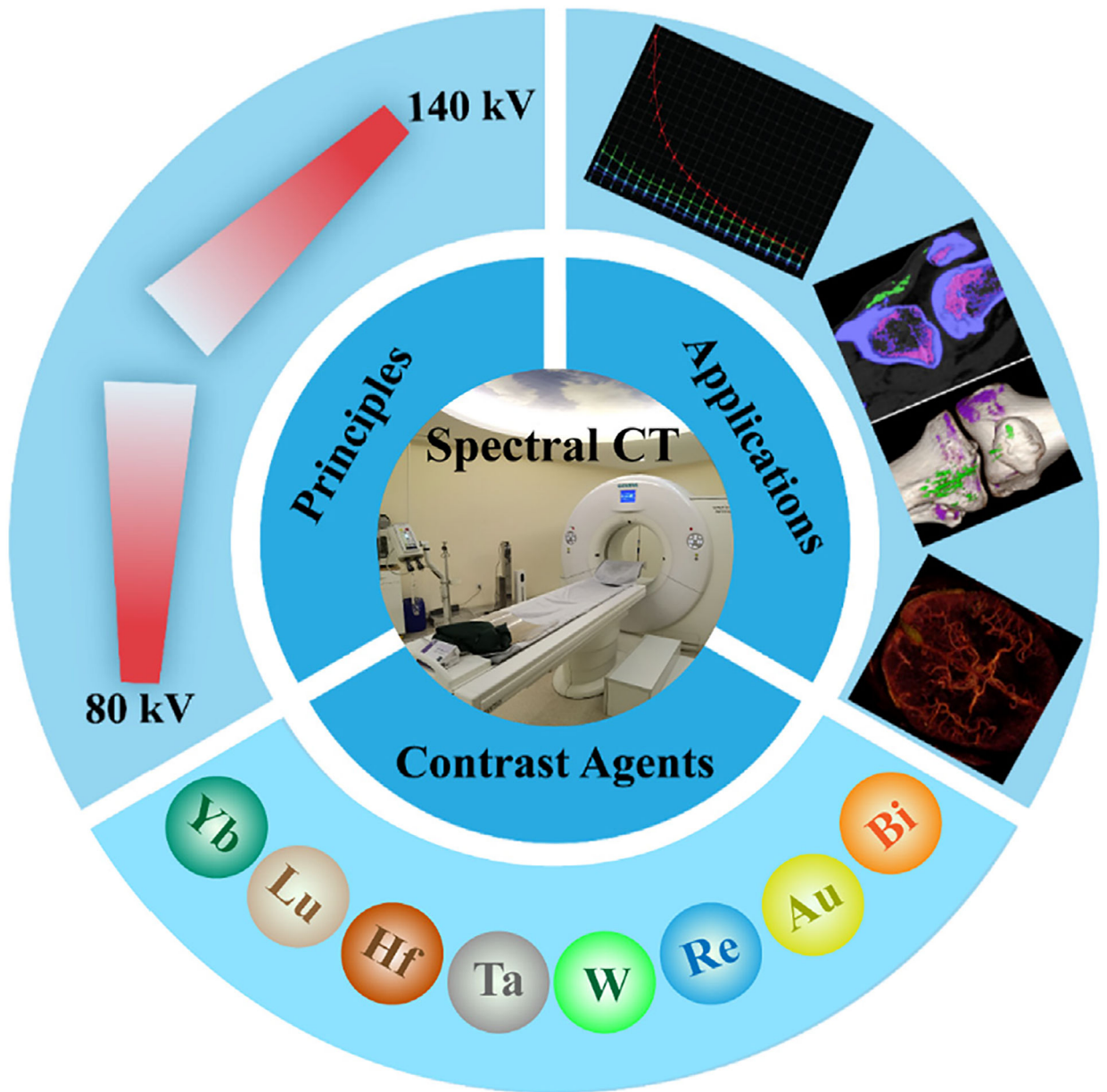
Fig. 1.
Illustration of the principles, applications and contrast agents of spectral CT.
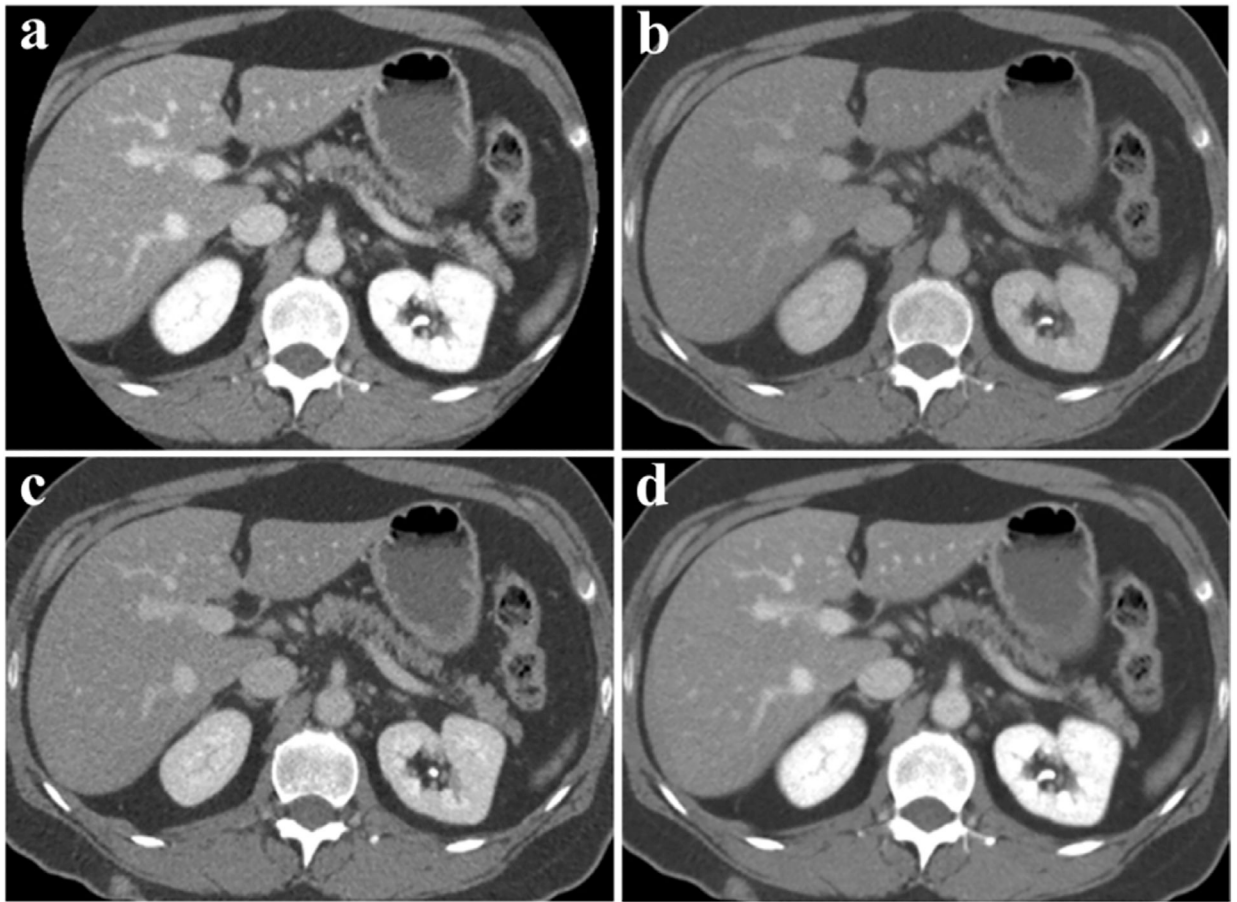
Fig. 2.
Clinical blending dual-energy CT images of the abdomen (Siemens Healthcare). a) 80 kVp.
b) 140 kVp. c) Linear mixing ratio 0.3 (The weight of 140 kVp is 70% and the weight of 80
kVp is 30%). d) Non-linear mixed image (Combines high contrast of 80 kVp and low noise
of 140 kVp images). Reproduced from Ref. [24] Copyright 2014, Radiology.
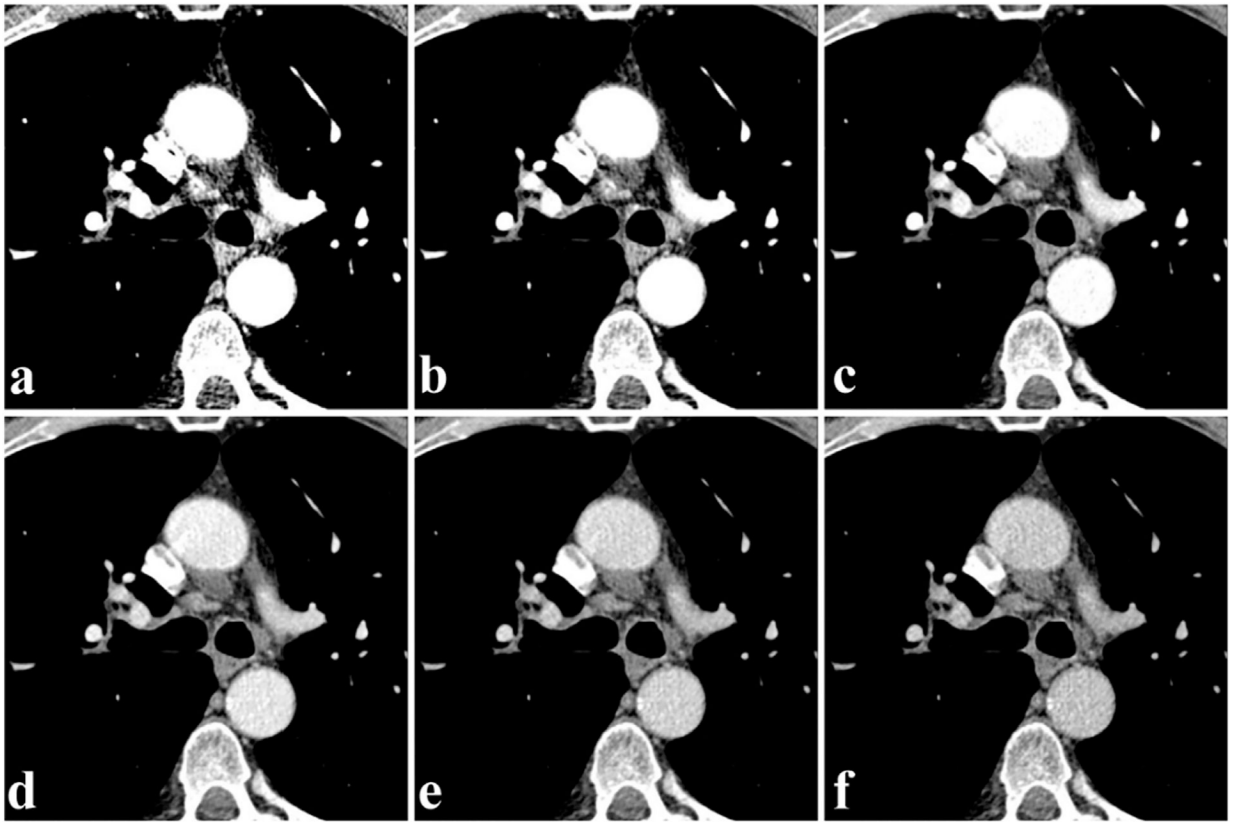
Fig. 3.
Dual-energy CT virtual monoenergetic image of the angiography cross section (Siemens Healthcare). a-f) Iodine-enhanced images at 50, 60, 70, 80, 90, and 100 keV, respectively. Reproduced from Ref. [52] Copyright 2013, Radiology.
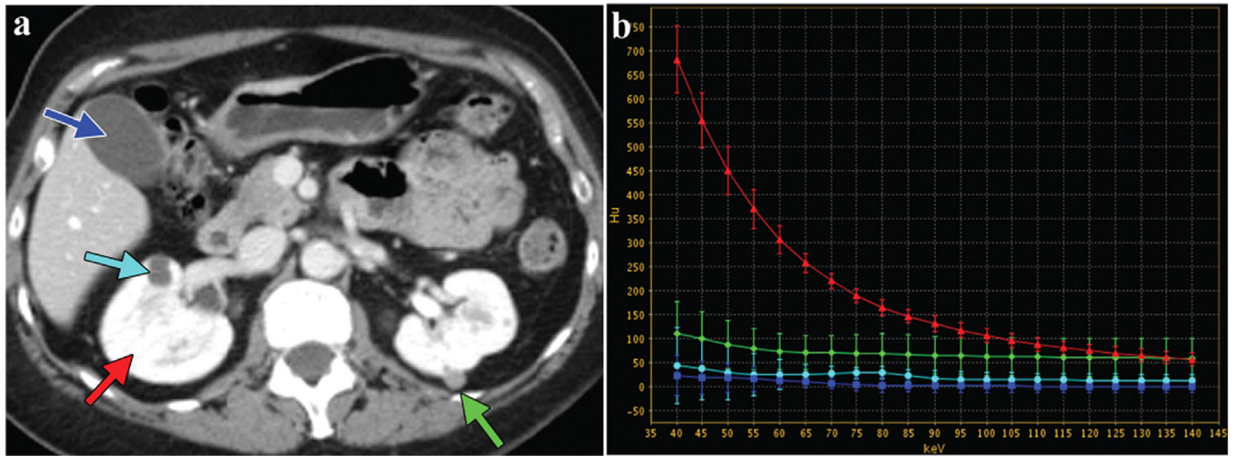
Fig. 4.
Dual-energy CT image of the abdomen (GE Healthcare). a) Abdominal cross section (The green arrow represents high-density lesion of left kidney; the light blue arrow is low-density lesion of right kidney; the red arrow is normal kidney enhancement; the deep blue is normal gallbladder fluid). b) Energy spectrum curves of different ROI. Reproduced from Ref. [13] Copyright 2011, RadioGraphics.
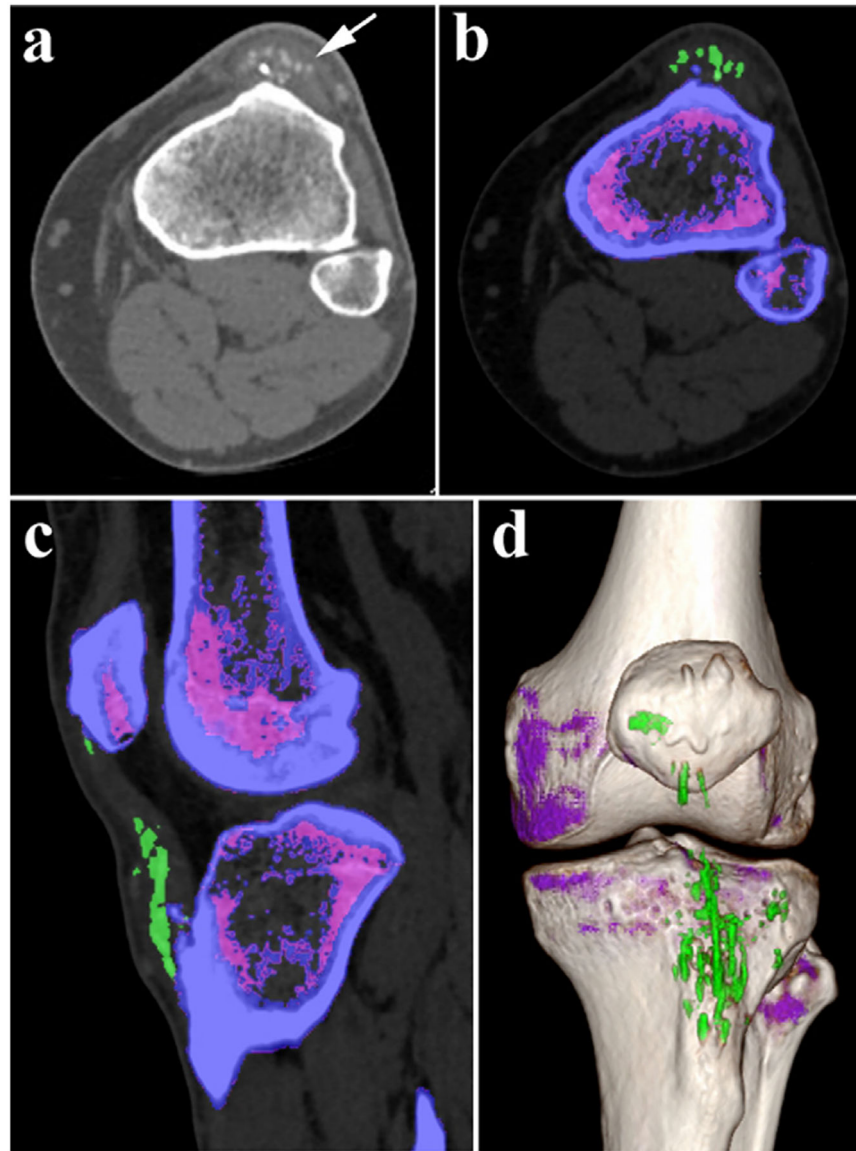
Fig. 5.
Dual-energy CT BMD image of left tibia (Siemens Healthcare). a) Gray image on conventional CT scans. b-d) Color image after gout procedure on DECT (the green represents uric acid, and the purple represents no uric acid). b) Cross section. c) Sagittal section. d) 3D reconstruction. Reproduced from Ref. [58] Copyright 2016, Radiology.
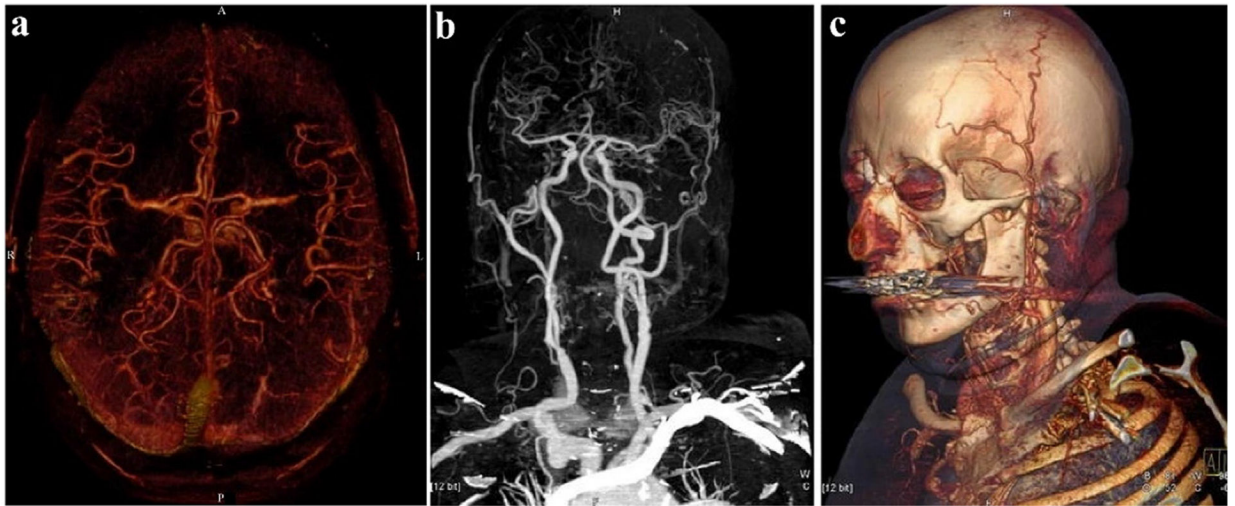
Fig. 6.
Angiography and 3D reconstruction images of the aorta (Siemens Healthcare). a) Observe the angiography from the axial (color image). b) Angiography of the aorta from coronal angle (gray image). c) 3D reconstruction (MPR). Reproduced from Ref. [25] Copyright 2006, European Radiology.
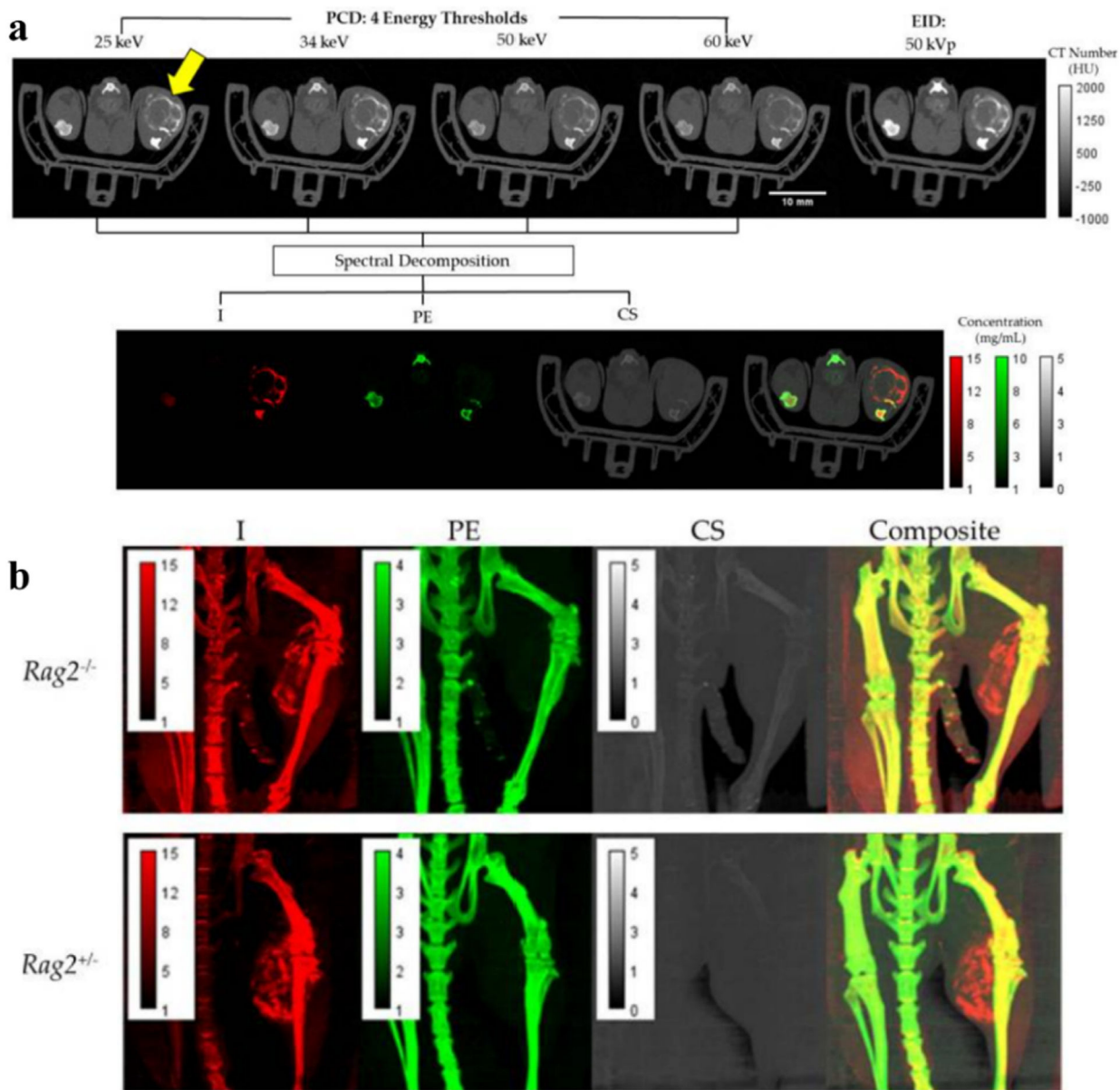
Fig. 7.
Studies on Lip-I CAs. a) Axial views of Rag2^{+/−} mouse. The first row shows CT color images of PCD and EID, and the second row shows material decomposition images (I, PE, CS). Yellow arrows indicate tumor areas. b) Coronal images (I, PE, CS, Composite) of Rag2^{−/−} and Rag2^{+/−} mouse. Reproduced from Ref. [101] Copyright 2022, Tomography.
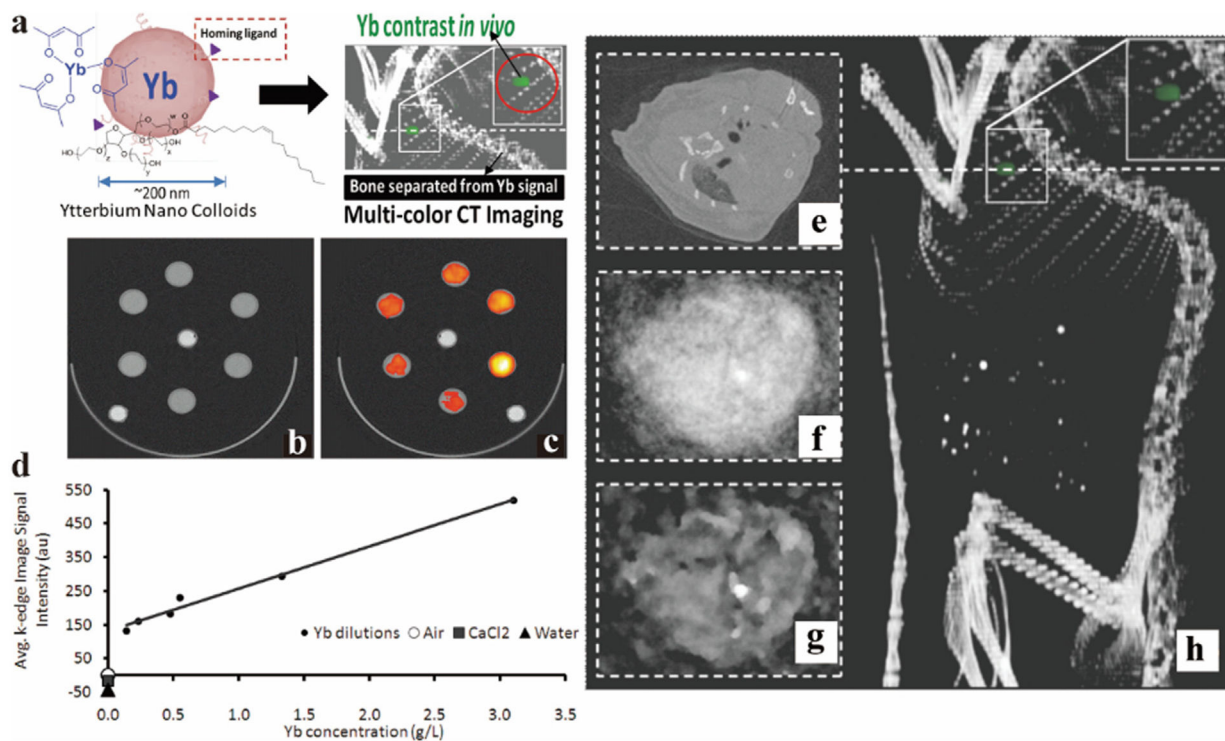
Fig. 8.
Studies on Yb-based NC CAs. a) Synthesis schematic of YbNC. b) Traditional CT images of diluted solutions of Yb, agarose and calcium chloride in the test tubes, respectively. c) Quantitative image of spectral CT (yellow represents higher Yb concentration, red represents lower concentration). d) Linear curve of Yb concentration measured value by spectral CT and ICP-OES. e-h) Blood pool image (heart cross section) of YbNC in traditional CT, normal image, iterative image, and 3D reconstruction of spectral CT (Philips Healthcare). Reproduced from Ref. [123] Copyright 2012, ACS Nano.
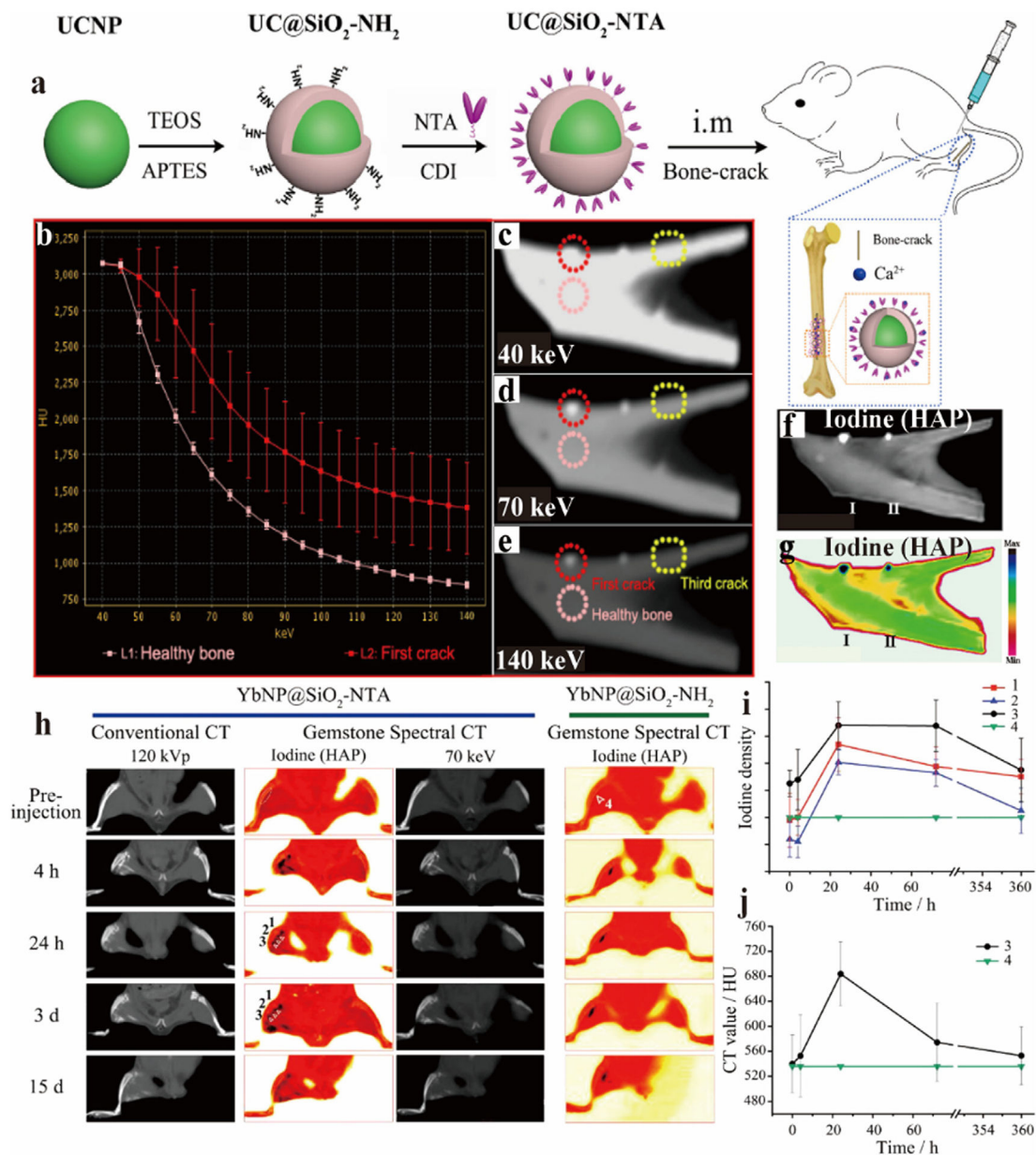
Fig. 9.
Studies on Yb-based NPs (YbNP@SiO$_2$-NTA) CAs. a) Sketch map of synthesis of UCNP@SiO$_2$-NTA. b) X-ray attenuation curves of healthy and cracked bone. c-e) Spectral CT images of cracked bones *in vitro* at 40 keV, 70 keV, 140 keV. f, g) iodine base image (gray and color). h) Conventional CT and spectral CT images at different times after intramuscular injection of YbNP@SiO$_2$-NTA and YbNP@SiO$_2$-NH$_2$. i) Curves of iodine density with against time at different bone locations. j) Curves of CT values with different times at different bone locations (GE Healthcare). Reproduced from Ref. [125] Copyright 2016, ACS Nano.
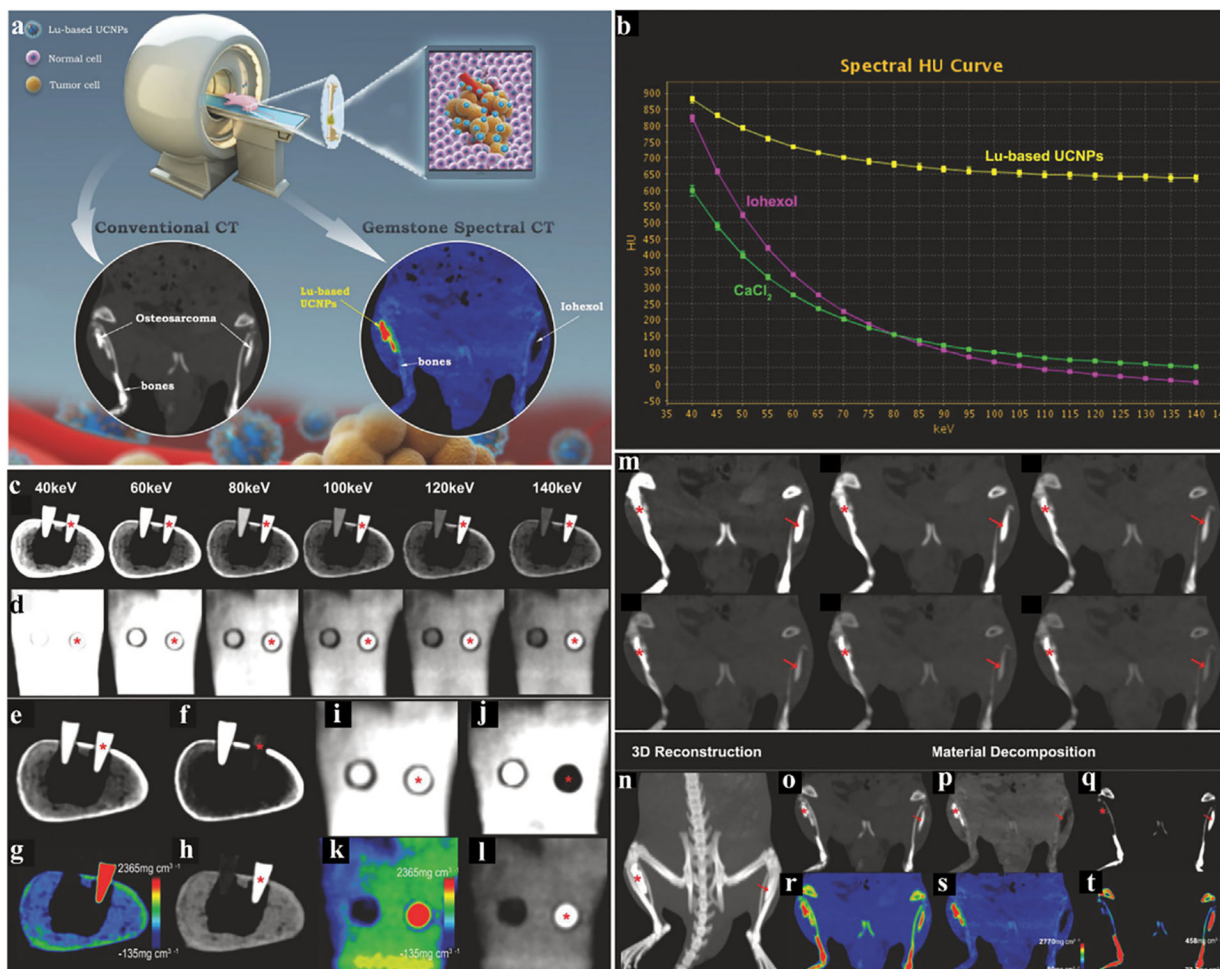
Fig. 10.
Studies on Lu-based UCNPs CAs. a) Schematic diagram of the study. b) X-ray attenuation curve of Lu-based UCNPs, iohexol, and $CaCl_2$. c, d) Images of bone, Lu-based UCNPs, and iohexol at different single energies (cross section, coronal section. Same below). e, i) Conventional CT images. f, j) The calcium (water) based gray image of GSCT. h, l) The water (calcium) based gray image of GSCT. g, k) The water (calcium) based color image of GSCT. m) The GSCT images of rats, half-body at 40, 60, 80, 100, 120, 140 keV respectively. n) The 3D reconstructed image of m). o, r) The conventional CT image (gray, color. Same below). p, s) The water (calcium) based image of GSCT. q, t) The calcium (water) based image of GSCT. All the red stars represent Lu-UCNPs, and the red arrows represent iohexol (GE Healthcare). Reproduced from Ref. [129] Copyright 2018, Advanced Functional Materials.
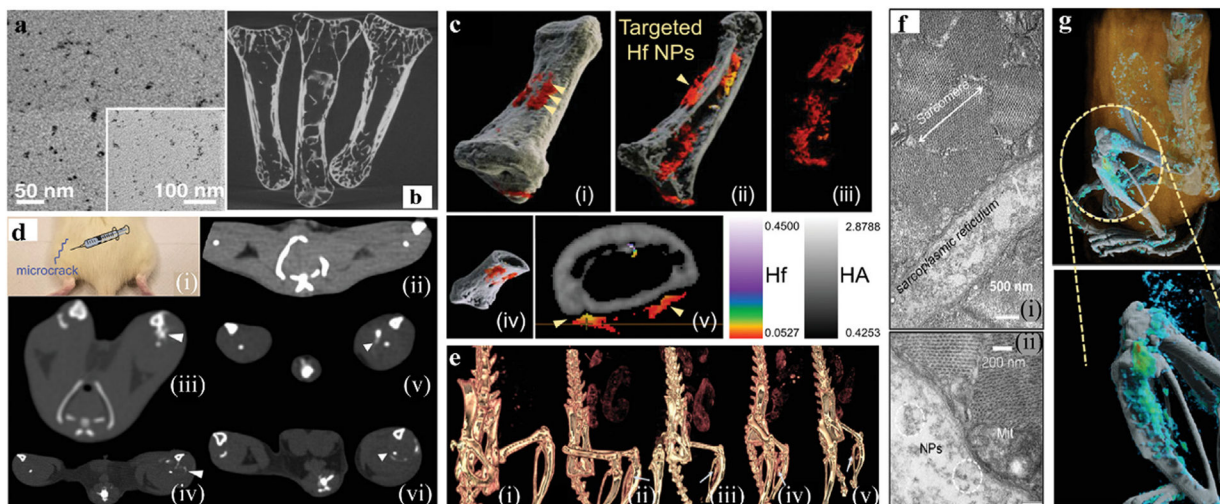
Fig. 11.
Studies on Hf-based NPs CAs. a) TEM image of HfO$_2$@NTA. b) micro-CT image of injured bone *in vitro*. c) i-v) The 3D reconstruction spectral CT image of HfNPs targeting injured bone *in vitro*. d) Rat model of induced bone injury i). Traditional CT images for ii) surgical without injection control group, iii-iv) the non-targeted injection group at 30 min and 5 h, respectively, v-vi) the targeted injection group at 30 min and 5 h, respectively. e) 3D images of ii-vi) in (d). f) TEM image of dissected muscle; (i) and (ii) are identical except for magnification. g) 3D reconstructed spectral CT images of targeted group (high concentration of Hf is marked in cyan-green, low concentration in blue and calcium channel in white) (GE Healthcare). Reproduced from Ref. [132] Copyright 2019, Advanced Functional Materials.
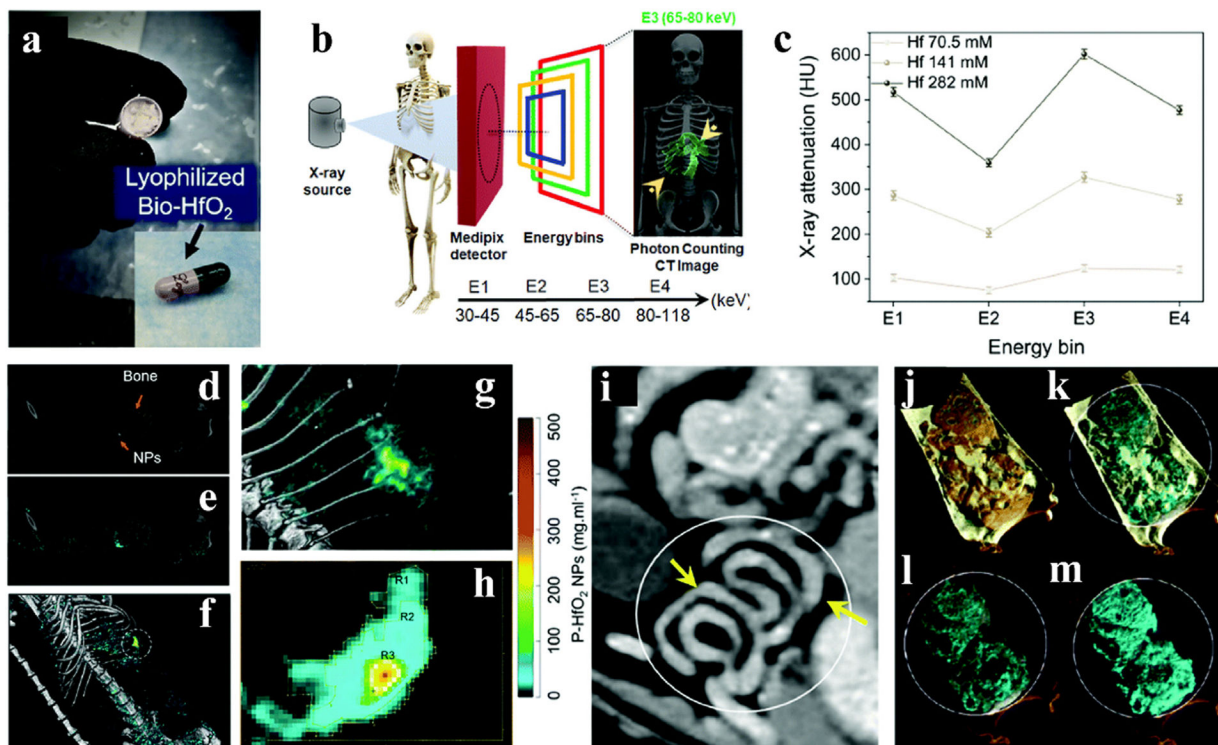
Fig. 12.
GI studies on HfO_2 NPs CAs. a) HfO_2 and probiotics were freeze dried and packaged in capsules. b) Schematic diagram of photon counting CT work. c) Spectral response graph of HfO_2. d) Coronal view of the energy bin in the rat. e) Coronal view of the energy bin overlaid with Hf in the rat. f) 3D reconstructed image of material decomposition. g) and h) Enlarged view of the area circled in f). The concentrations in the R1, R2 and R3 regions range from low to high, respectively. i) Photon-counting CT images of the GI tract without fasting before gavage with Hf capsules. j-m) Partial enlarged view of the lining of the GI tract in i). Soft tissue (orange), lipid (yellow), HA (gray) and HfO_2 NPs (cyan) (small-bore MARS spectral CT scanner). Reproduced from Ref. [133] Copyright 2022, Nanoscale Horizons.
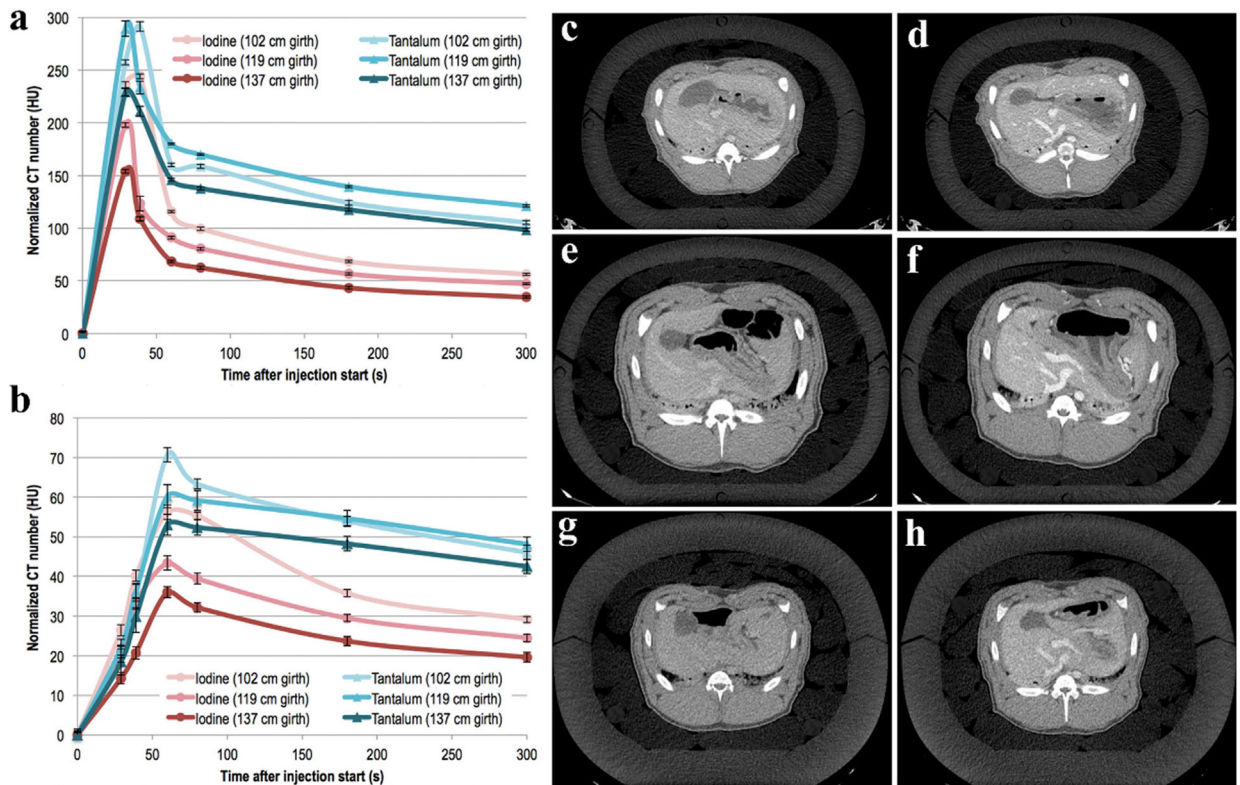
Fig. 13.
Studies on Ta-based NPs CA. a, b) Mean CT values of iopromide and TaNPs for three size perimeters in the abdominal aorta and liver, respectively. Axial CT images of liver with iopromide (left) and TaNPs (right) at a circumference of c,d) 102, e,f) 119, g,h) 137 cm (GE Healthcare). Reproduced from Ref. [137] Copyright 2018, Radiology.
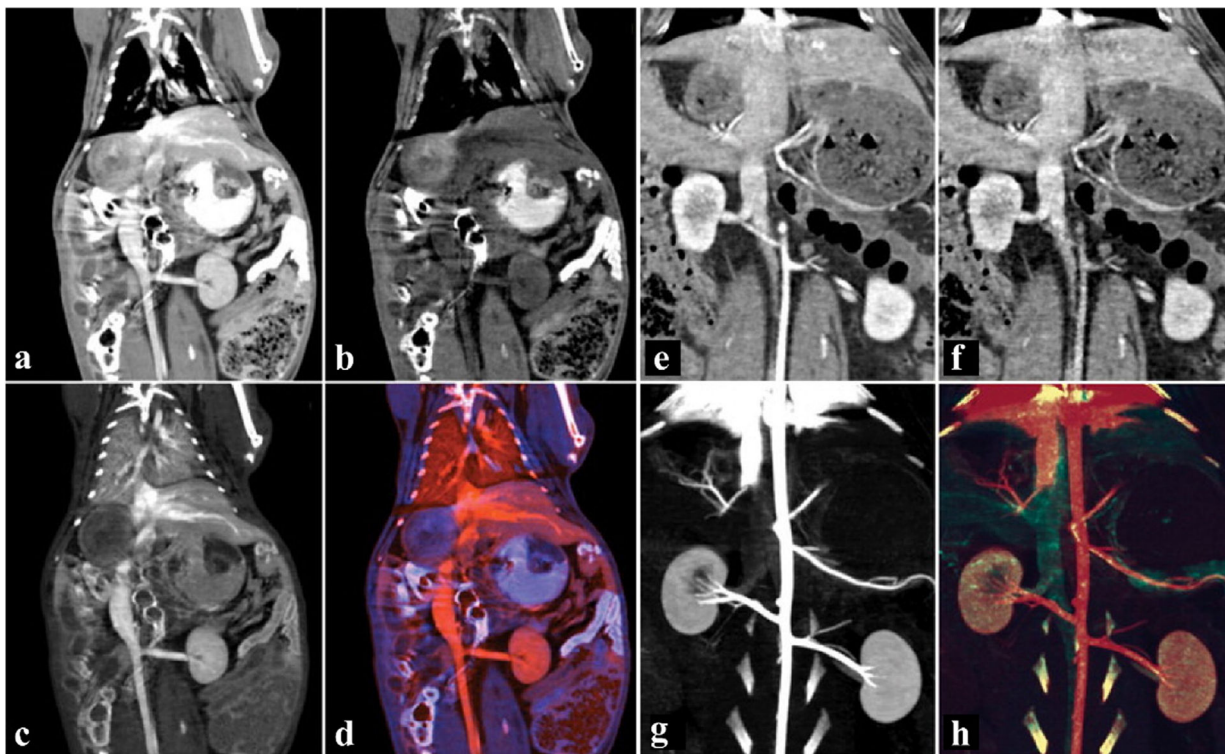
Fig. 14.
Studies on tungsten NPs CAs. a-d) Coronal images of the abdomen with bismuth-based and I-based CAs. a) Virtual monochromatic image at 70 keV. b) Bismuth material map. c) I material map. d) The overlaid color map of bismuth and I. e-h) Angiographic coronal image of the abdomen with W-based and I-based CAs. e) Virtual monochromatic image at 140 keV. f) W material map. g) I material map. h) The overlaid color map of W and I (The red area is iodine, the blue-purple area is bismuth, and the green area is W) (GE Healthcare). Reproduced from Ref. [140] Copyright 2012, Radiology.
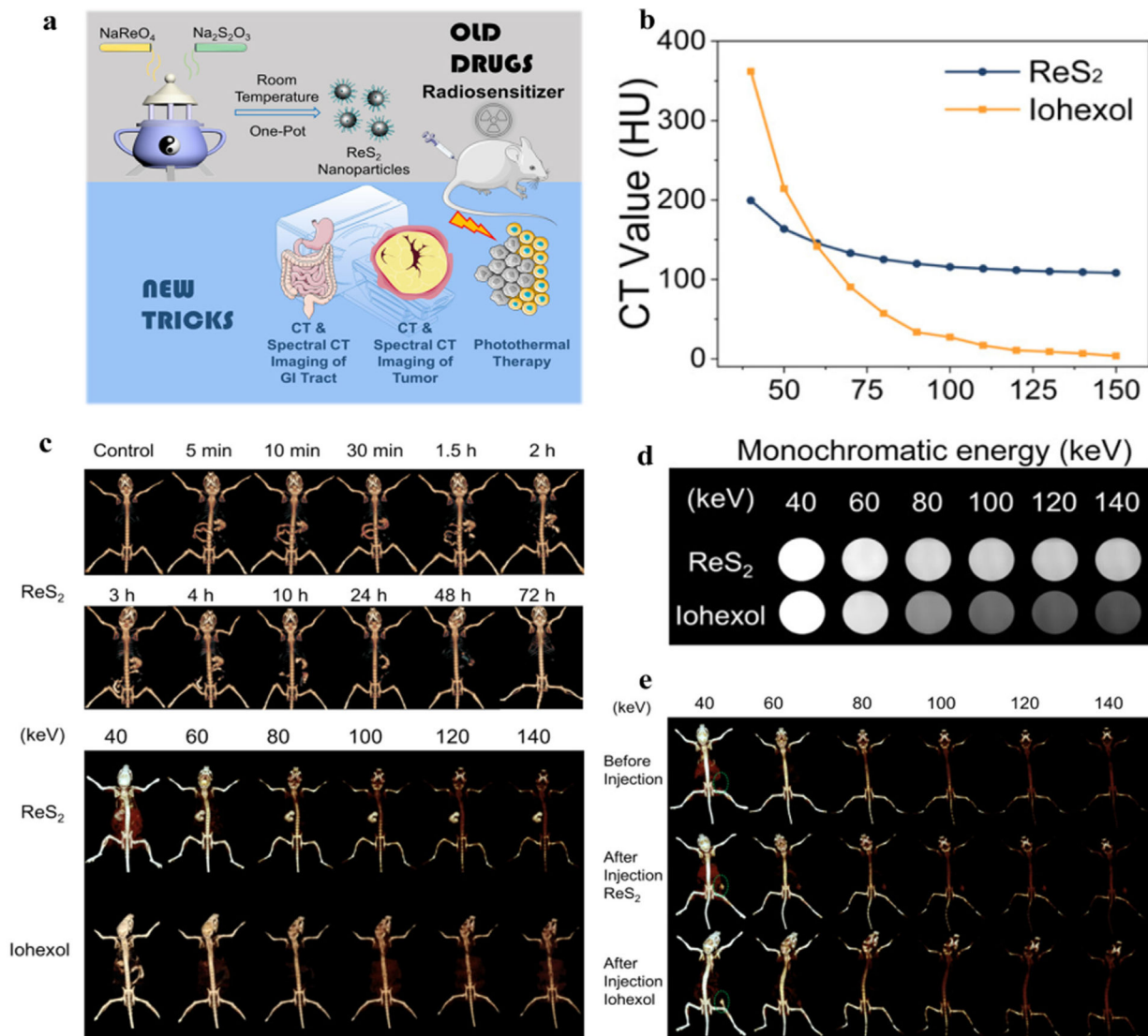
Fig. 15.
Studies on Re-based NPs CAs. a) Schematic representation of ReS_2 NPs. b) The X-ray attenuation curve of ReS_2 and iohexol. c) The spectral CT image of the GI system at different times after oral administration of ReS_2 (above) and different keV image after oral administration of ReS_2 and iohexol at 5 min (below). d) Gray spectral CT image of ReS_2 and iohexol at different keV. e) The spectral CT image at different keV before and after intratumoral injection of ReS_2 and iohexol *in vivo* (Siemens Healthcare). Reproduced from Ref. [143] Copyright 2019, ACS Applied Materials & Interfaces.
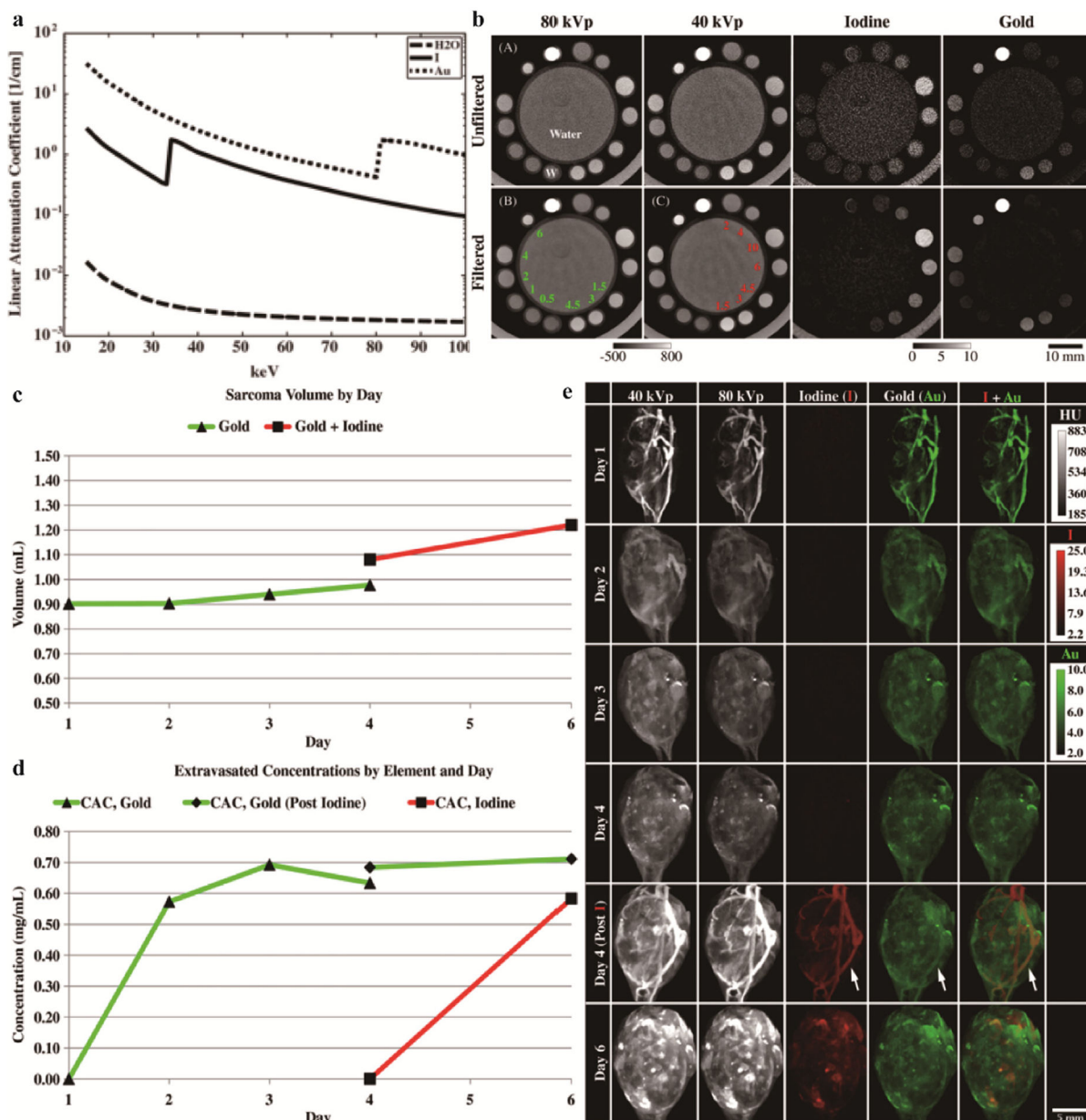
Fig. 16.
Studies on Lip-I and Au-based NPs CAs. a) The K-edge energy of water, iodine, and Au. b) Decomposition ability of DE *in vitro*. Water, iodine and Au were placed respectively, and the unit is mg/mL. The CT value and quantitative analysis concentration are marked with gray scale below the image. c) Tumor volume calculated by manual delineation. d) DE micro-CT calculates element extravasation concentrations. e) DE micro-CT images of 40 kVp, 80 kVp, iodine, Au, and iodine overlaid with Au. Measured on days 1 thru 6. The Au was injected on the first day and the iodine on the fourth day. Reproduced from Ref. [155] Copyright 2013, Physics in Medicine & Biology.
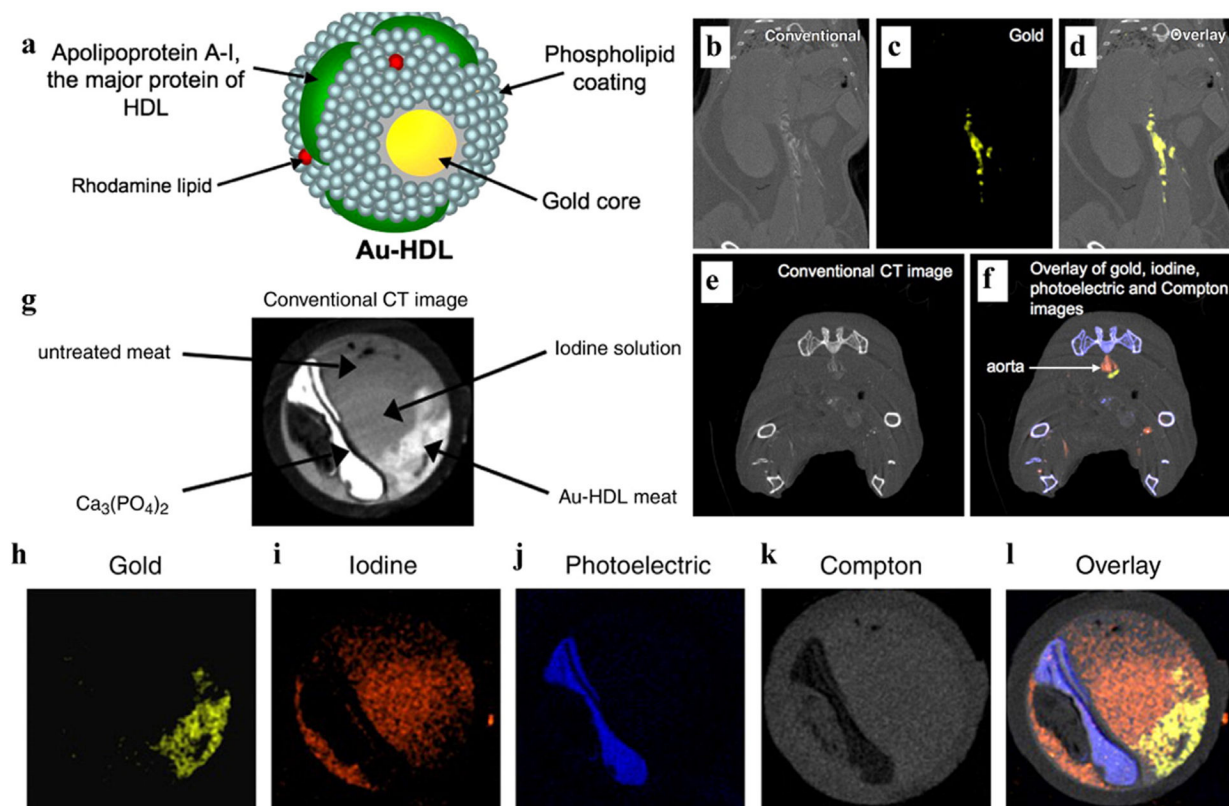
Fig. 17.
Studies on Au-based NPs (Au-HDL) CAs. a) Schematic diagram of Au-HDL. b-d)
Conventional, gold and overlay image of a mouse, 24 h after Au-HDL injection. e-f)
Conventional CT hybrid images and spectral CT hybrid images of Au-HDL and iodinated
CAs. g) Traditional CT images of an *in vitro* model. h-l) The gold, iodine, photoelectric
effect, Compton effect, and overlay spectral images *in vitro* (Philips Healthcare).
Reproduced from Ref. [158] Copyright 2010, Radiology.
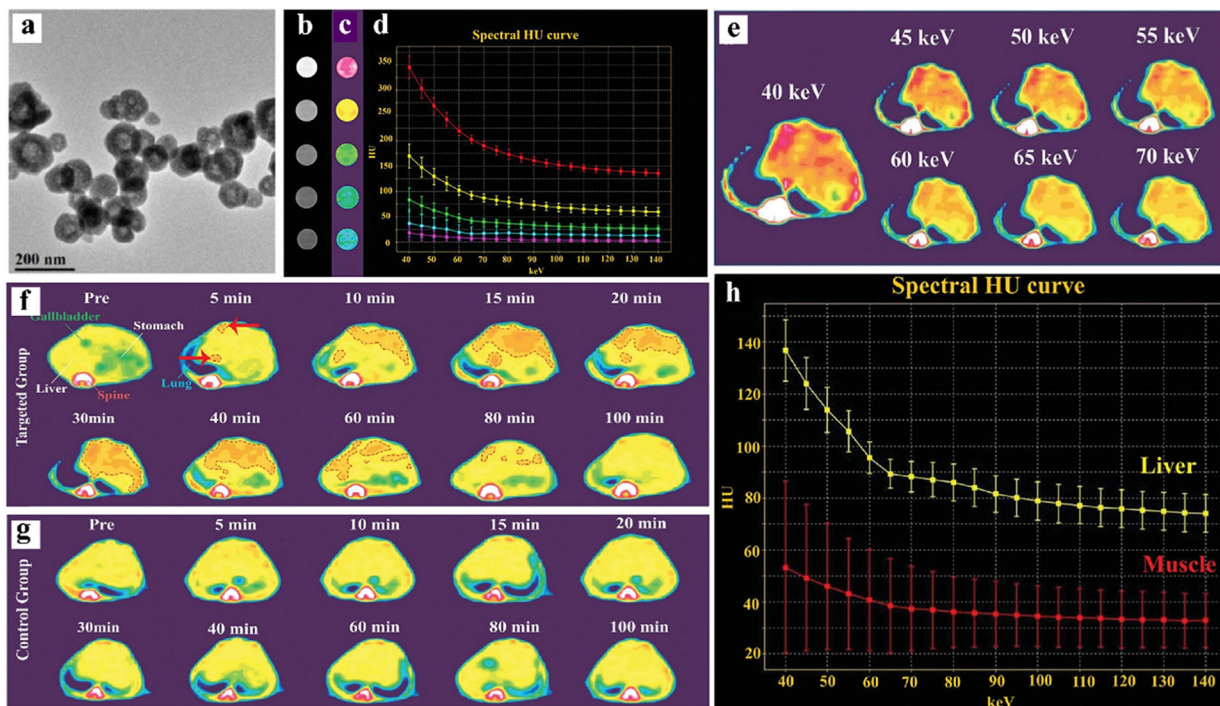
Fig. 18.

Studies on Bi-based NPs (BiF$_3$@PDA@HA) CAs. a) TEM of BiF$_3$@PDA@HA. b) Conventional CT image of Bi-based NPs. c) Color images of Bi-based NPs measured by GSCT.d) X-ray attenuation curves of different concentrations. Top down, the Bi concentration is 10000, 5000, 2500, 1250, and 625 μg/mL. e) The GSCT images of the targeted group at different keV, 30 min after injection. f) The GSCT images of the targeted group at different times after injection. g) The GSCT images of the control group at different times after injection. h) X-ray attenuation curve of liver and normal muscle in targeted group 30 min after injection (GE Healthcare). Reproduced from Ref. [202] Copyright 2021, Advanced Science.
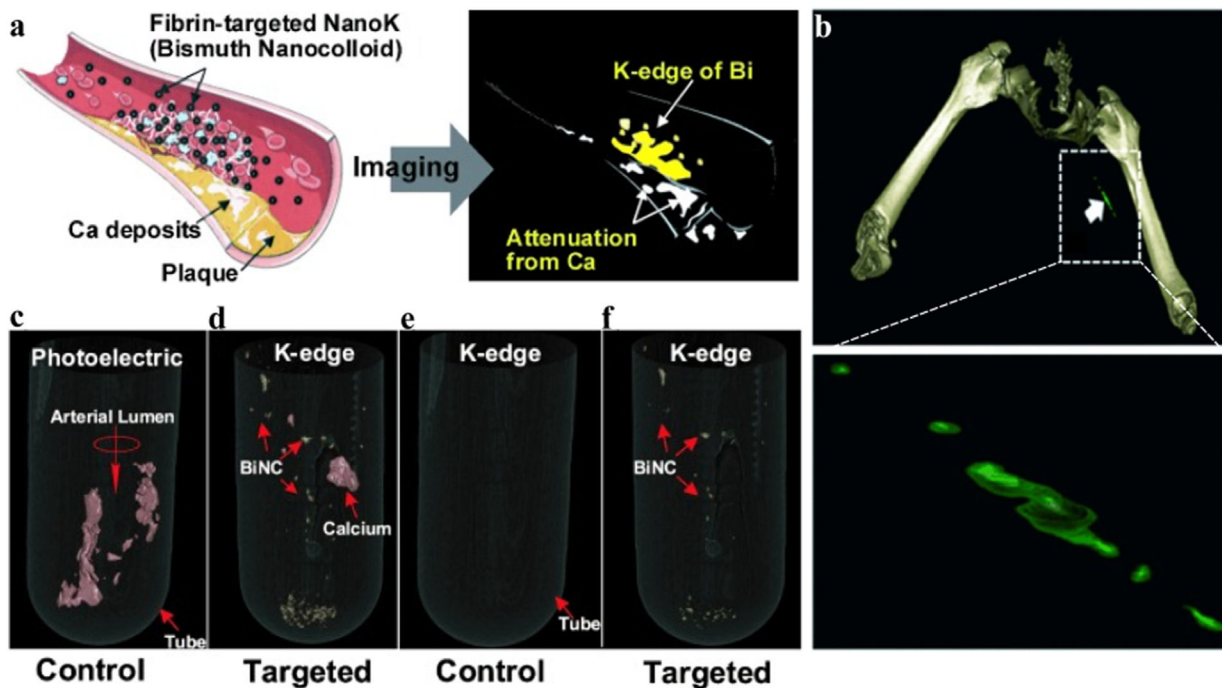
Fig. 19.
Studies on Bi-based nanocolloid CAs. a) Schematic representation of Nano-K targets
arteriosclerosis and imaging. b) The spectral CT image of Nano-K targeting rabbit thrombus
(max clot diameter is 1.41 mm, min clot diameter is 1.25 mm). c, e) Spectral CT images
of control group (ConNC without Bi) co-incubated with human carotid artery specimens
(calcium signal is red, NanoK signal is gold). d, f) Spectral CT images of the targeted
group (NanoK) co-incubated with human carotid artery specimens (Philips Healthcare).
Reproduced from Ref. [203] Copyright 2010, Angewandte Chemie-International Edition.

Table 1

Technical Approaches to Acquire Dual-Energy Images.

Dual- and multi-energy CT technology	Schematic diagram of scanning method
Sequential scans	
Rapid switching of the single X-ray tube	
Single X-ray tube and double detector	
Double X-ray tube and double detector	
Photon counting detectors	

Table 2

Information of candidate elements for DECT or spectral CT CAs.

Atomic number	Name	K-edge (keV)	Nanoparticle	Applications of elements
53	Iodine (I)	33.2	iohexol, ioversol, iopromide, iopamidol	CT
70	Ytterbium (Yb)	61.3	YbNC, YbNP@SiO$_2$-NTA	CT/ Upconversion luminescence imaging
71	Lutetium (Lu)	63.3	(PEG)-NaLuF4:19 % Yb^{3+}/1% Er^{3+}	CT/ Upconversion luminescence imaging
72	Hafnium (Hf)	65.3	HfO$_2$	CT
73	Tantalum (Ta)	67.4	Zwitterionic-coated tantalum oxide (TaCZ)	CT
74	Tungsten (W)	69.5	NMG$^+$[(W$_3$O$_2$)(acetylate)$_9$]$^-$ (tungsten cluster)	CT/ Photothermal therapy (PTT)
75	Rhenium (Re)	71.7	ReS$_2$	CT/PTT
79	Gold (Au)	80.7	AuNP, Au-HDL	CT/PTT/ Chemotherapy
83	Bismuth (Bi)	90.5	BiF$_3$@PDA@HA, Fibrin-targeted BiNC	CT/PTT